

1 **Title**

2 Data assimilation of hyper-local water level sensors for real-time monitoring of coastal inundation

3

4 **Authors**

5 Youngjun Son ^{a,*}, Emanuele Di Lorenzo ^{a,b}, Kyungmin Park ^c, Spenser Wipperfurth ^a, and Jian Luo ^d

6

7 **Affiliations**

8 ^a *Program in Ocean Science and Engineering, Georgia Institute of Technology, Atlanta, GA, USA*

9 ^b *Department of Earth, Environmental, and Planetary Sciences, Brown University, Providence, RI, USA*

10 ^c *Coastal Sciences Division, Pacific Northwest National Laboratory, Seattle, WA, USA*

11 ^d *School of Civil and Environmental Engineering, Georgia Institute of Technology, Atlanta, GA, USA*

12 ^{*} *Corresponding Author*

- 13 • E-mail address: youngjun.son@gatech.edu (Y. Son)

- 14 • Address: *311 Ferst Drive, Atlanta, GA, USA, 30332*

15

16 **Submitted to**

17 *Coastal Engineering*

18

19 **Highlights**

- 20 • Objective Analysis is implemented to reconstruct water levels from sensor observations.
- 21 • Spatial covariance statistics are derived from coastal-ocean hydrodynamic model simulations.
- 22 • Variability in water levels is better captured by combining spatial covariance information.
- 23 • Real-time assimilation can provide situational awareness of floods in coastal communities.

24

25 **Abstract**

26 As flood events become increasingly prevalent in coastal regions with sea level rise, multiple
27 communities have deployed water level monitoring networks across estuaries in addition to existing tide
28 gauges located primarily at immediate coasts. Due to the spatially-distributed nature of sensor
29 deployments, however, water level data are only available at specific sensor locations during the time of
30 monitoring. As a result, an information gap on water levels exists along estuarine channels outside of
31 active monitoring locations. To fill such a gap, this study presents a physics-based empirical modeling
32 approach to assimilate coastal water levels using observations from hyper-local water level sensors. We
33 implement an Objective Analysis (OA) procedure for sensor observation datasets obtained from the Smart
34 Sea Level Sensors project along the U.S. Georgia coasts, based on spatial covariance structures of water
35 levels that are extracted from high-resolution coastal-ocean hydrodynamic simulations. The approach is
36 validated using simulated water levels, which provide basis functions for spatial covariance information.
37 Additionally, the implementation is validated using actual water levels from active monitoring stations.
38 The assimilated results of water levels are compared to those obtained by the same OA procedure but
39 with a commonly-used Gaussian covariance function, which lacks prior knowledge of spatial covariance
40 structures. To demonstrate the capability of the assimilation approach, we extend its application to a
41 hurricane event, during which other dynamic processes may be relevant to variability in coastal water
42 levels. Overall, the presented approach provides an accurate and efficient estimation of estuarine water
43 levels along channels, which can support community officials to promptly identify localized flood threats
44 to critical infrastructure systems in coastal regions.

45

46 **Keywords**

47 coastal flood; water level; data assimilation; objective analysis; monitoring network; hyper-local sensor

49 **1. Introduction**

50 Flooding is a growing threat to both populations and infrastructure in coastal regions (Hallegatte et al.,
51 2013; National Academies, 2014; Allen et al., 2018). Primarily produced by a tropical storm or hurricane,
52 a storm surge can cause catastrophic flooding and subsequent damages along coastlines, including human
53 causalities and property losses (Grinsted et al., 2019). In addition, sea level rise due to climate change
54 further exposes a greater number of coastal communities to an increased risk of flooding during high tides
55 (Muis et al., 2016; Sweet et al., 2022). Over the last several decades, for example, the average number of
56 high tide flood days per year has been steadily increasing in major cities and towns along the U.S. coasts,
57 more than doubling particularly along the Southeast Atlantic coasts (Sweet et al., 2018; Moore and
58 Obradovich, 2020). Recurrent flooding leads to public inconvenience and mental distress by repeatedly
59 disrupting local transportation and business in low-lying urban areas (Moftakhari et al., 2015). Moreover,
60 high tide flooding poses a significant risk to infrastructure systems in coastal regions, such as bridges,
61 marinas, and stormwater drainages (Tahvildari and Castrucci, 2021; Gold et al., 2022). These structures
62 could temporarily fail to function and even permanently lose structural integrity due to inundation by
63 saline floodwater (Allen et al., 2018). Unfortunately, coastal infrastructure has limited adaptive capacity
64 to cope with sea level rise and consequent flood impact due to restricted relocation options. Therefore,
65 obtaining reliable information on water levels along major channels becomes crucial, not only for
66 monitoring imminent flood threats but also for facilitating long-term planning to enhance flood resilience.

67 In many coastal regions, public and emergency management officials rely on real-time tide
68 observations at a sparse network of NOAA stations, even though monitoring points of interest may be
69 several kilometers away from the nearest station. In estuaries, however, water levels result from rising and
70 falling tides and interactions with a range of channels from rivers to tributaries, landscapes, and local
71 meteorological disturbance, which generate a complex pattern along coastlines (Gallien et al., 2011;
72 Marsooli et al., 2016; Bilskie et al., 2021). Although advances in coastal-ocean modeling techniques have
73 facilitated extreme water level predictions associated with hurricane-induced storm surges, operational
74 forecasts using high-resolution models can incur high computational costs (Kerr et al., 2013; Bilskie et al.,
75 2020). Moreover, multiple sources of uncertainties originating from input topobathymetry and boundary-
76 forcing conditions cause gaps between model predictions and actual observations (Muñoz et al., 2022),
77 which persist and propagate over simulation periods. Without leveraging gauge-based observations
78 through model calibration or data assimilation, physics-based model predictions remain limited to
79 assisting community officials in identifying immediate flood threats in coastal regions.

80 Recently, several coastal communities have been deploying affordable water level sensors in an
81 urgent effort to obtain real-time water level information and better understand the hyper-local impacts of
82 rising sea levels. As summarized in Table 1, multiple monitoring networks have been established along

83 the U.S. coasts, using low-cost water level sensors by local researchers and communities. The sensor
 84 devices can measure water levels based on pressure, radar, and ultrasonic techniques and transmit
 85 measured data via long-range radio, cellular, or satellite communication. In the City of Norfolk, U.S.
 86 Virginia, for example, the StormSense project (Loftis et al., 2018) has deployed more than 50 water level
 87 sensors, either radar- or ultrasonic-type, to spatially complement the existing NOAA tide gauges and
 88 support predictive flood modeling. Another example is the Smart Sea Level Sensors (SSLS) project,
 89 which has installed more than 60 ultrasonic water level sensors along the U.S. Georgia coasts to augment
 90 hyper-local water level monitoring, with high priority to locations of critical infrastructure systems, such
 91 as bridges and boat ramps. These monitoring networks allow public and emergency management
 92 professionals to access hyper-local water level conditions and take prompt actions in response to potential
 93 flood risks. However, available monitoring locations are still confined by finite sensor installations (Tien
 94 et al., 2023). Furthermore, the observation availability is influenced by sensor operation that is subject to
 95 power supply or weather conditions for wireless communications. For example, sensors may cease to
 96 function due to power loss or faulty instruments, resulting in a lack of access to vital water level data,
 97 particularly during precarious events such as spring tides. Given these constraints, real-time assimilation
 98 of water level observations becomes crucial as it can facilitate extensive support for expanding sensor
 99 networks by estimating water levels at inactive sensor locations and in geographic areas beyond the
 100 immediate vicinity of sensor installations.

101 **Table 1**
 102 Water level monitoring networks using low-cost, power-efficient sensors along the U.S. coasts.

Project	Location	Number of Sensors	Sensor Type	Primary Network Communication	Observation Availability*	Observation Cycle	Reference
StormSense	Norfolk, Virginia	50 +	Ultrasonic and Radar	Cellular and RoLaWAN	2016 to Present	6-minute	Loftis et al. (2018)
Smart Sea Level Sensors (SSLS)	Georgia	60 +	Ultrasonic	RoLaWAN	2019 to Present	6-minute	https://www.sealevelsensors.org/
Hohonu	U.S. East Coast, Hawaii, and Alaska	90 +	Ultrasonic	Cellular	2017 to Present	6-minute	https://www.hohonu.io/
SenseStream (I-SENSE)	Florida and South Carolina	50 +	Ultrasonic	Cellular	2018 to Present	5-minute	https://www.sensestream.org/
Sensing Storm Surge	Maine	20 +	Pressure	Not capable	2017 to 2020	2-minute	Spicer et al. (2021)

* Observation availability varies depending on the deployment and operation of individual water level sensors.

103 Due to a short history of hyper-local water level monitoring networks, no prior study exists to
 104 assimilate coastal water levels directly from the newly emerging observation datasets. At global- or
 105 regional-scales in oceanography, however, many studies have been conducted to reconstruct a large-scale
 106 map of oceanographic data based on observations with limited spatial coverage. Since the introduction

107 into oceanography by Bretherton et al. (1976), the Objective Analysis (OA) technique has been
108 extensively used to interpolate spatial sampling data into a continuous field of ocean properties, including
109 sea surface height (e.g., Ubelmann et al., 2015), temperature (e.g., Smith et al., 1996), and pressure (e.g.,
110 Kaplan et al., 2000). Smith et al. (1996) were the first to utilize Empirical Orthogonal Functions (EOFs)
111 for spatial covariance statistics to fill spatial gaps in marine observations of sea surface temperature, using
112 satellite-based datasets with extensive coverage. Similarly, Chambers et al. (2002) applied EOFs that
113 were derived from satellite altimetry into historical tide gauge records to examine the effects of climate
114 variability on global mean sea levels. To assess an emerging risk of floods in the context of a changing
115 climate, the EOFs-based OA technique has been widely adopted in identifying global and regional
116 variability in rising sea level trends (e.g., Church and White, 2006; Hamlington et al., 2012). The
117 application has been further improved by reducing inherent uncertainties in observation datasets (e.g.,
118 Church et al., 2004; Church and White, 2006), by applying sophisticated basis functions, such as
119 cyclostationary EOFs (e.g., Hamlington et al., 2011; Kim et al., 2015), or by combining with other
120 climate variables (e.g., Hamlington et al., 2012; Kumar et al., 2020). Ocean circulation model simulations
121 have also been used as an alternative to satellite altimetry datasets to derive the spatial patterns of
122 physical ocean systems (e.g., Llovel et al., 2009; Meyssignac et al., 2011). Although the primary focus of
123 these studies has been on estimating variability of sea level rise trends at large spatiotemporal scales, the
124 application of the EOFs-based OA technique has enabled the reconstruction of water levels by combining
125 spatial covariance structures with scattered observation datasets.

126 In studies related to coastal floods, the EOF analysis has been frequently employed for
127 dimensionality reduction within surrogate models, which are commonly referred to as metamodels. For
128 coastal flood predictions, surrogate models build a functional connection between input parameters (e.g.,
129 hurricane intensity and track) and corresponding responses (e.g., maximum storm surge) based on
130 numerical model simulation databases for historical or synthetic flood events (Jia and Taflanidis, 2013; Al
131 Kajbaf and Bensi, 2020). To address the challenges posed by high-dimensional spatiotemporal outputs,
132 the EOF analysis not only reduces the dimensionality of output responses but also facilitates the
133 extraction of response covariance patterns (Jia and Taflanidis, 2013; Jia et al., 2015), as similarly applied
134 within the EOFs-based OA technique. In addition, various statistical representations, including Gaussian
135 Process Regression and Neural Networks, have been utilized in surrogate models to establish
136 relationships between the weights of response covariance patterns and metocean input parameters (see a
137 review in Al Kajbaf and Bensi, 2020). Specifically, surrogate models have been applied to different
138 coastal flood drivers, such as storm surge (e.g., Jia et al., 2015; Bass and Bedient, 2018; Rohmer et al.,
139 2023; Kyprioti et al., 2023), storm waves (e.g., Jia and Taflanidis, 2013; Rohmer et al., 2023), and even
140 tidal responses with elevated levees in estuaries (Li et al., 2020). On the other hand, the EOFs-based OA

141 technique directly leverages spatially-distributed response observations (i.e., water levels for coastal flood
142 monitoring) to determine the weights of response covariance patterns. Within the EOFs-based OA
143 technique, optimal interpolation (Daley, 1991; Kalnay, 2003) is a key component that generates the most
144 likely spatial state representation by minimizing error variances at observation locations. Regarded as a
145 specific suboptimal variant of the extended Kalman filter (Ide et al., 1997), optimal interpolation serves a
146 fundamental role in both real-time assimilation and sequential updates of forecast models due to its
147 relative simplicity (e.g., Madsen et al., 2015; Asher et al., 2019 to adjust storm surge model forecasts). As
148 water level observation datasets newly emerge at hyper-local scales for coastal flood monitoring, it
149 becomes increasingly relevant to explore their potential applications in data assimilation, especially with
150 established traditional methods such as the OA technique.

151 The objective of this study is to develop a physics-based empirical modeling approach to augment
152 water level monitoring of a hyper-local sensor network. To achieve this objective, we apply the OA
153 procedure to assimilate water levels in coastal regions, following a similar methodology used by
154 Chambers et al. (2002) to reconstruct mean sea levels globally. Particularly, coastal-ocean hydrodynamic
155 model simulations are performed to extract spatial covariance statistics of water levels which are then
156 decomposed in EOFs. As a result, past and present water levels can be assimilated by combining the
157 spatial covariance information with a time series of available sensor observations. Our study explores the
158 feasibility of the empirical modeling approach for hyper-local sensor observations which integrates spatial
159 covariance structures established from physics-based model simulations. In addition, we examine the
160 applicability of the modeling approach using a range of scenarios, including both tides to storm events.
161 As a computationally efficient and accessible option for real-time applications, the modeling approach
162 allows community officials to access hyper-local water level conditions, even for temporarily inoperative
163 sensor locations. Furthermore, the outcomes can provide valuable insights for optimizing the deployment
164 of sensors that are constrained by limited resources. Ultimately, the assimilated water levels can benefit
165 coastal-urban flood models that rely on accurate water level data along coastlines to predict flooding in
166 urban systems (e.g., Smith et al., 2011; Karamouz et al., 2017; Son et al., 2023).

167 The remainder of the paper is organized as follows. Section 2 describes the OA procedure that
168 combines physics-based model simulations, along with the background information on the hyper-local
169 water level monitoring network and the high-resolution coastal-ocean hydrodynamic model. In Section 3,
170 we examine the physics-based empirical modeling approach by using the numerical simulation results to
171 quantify the different sources of errors. Then, the applications are extended to assimilate water levels
172 directly using actual observations from the hyper-local sensor networks, not only for the basis simulation
173 periods but also for a hurricane event that occurred during the operational monitoring periods.
174 Furthermore, our study demonstrates the real-time assimilation of water levels in a pilot web-based portal

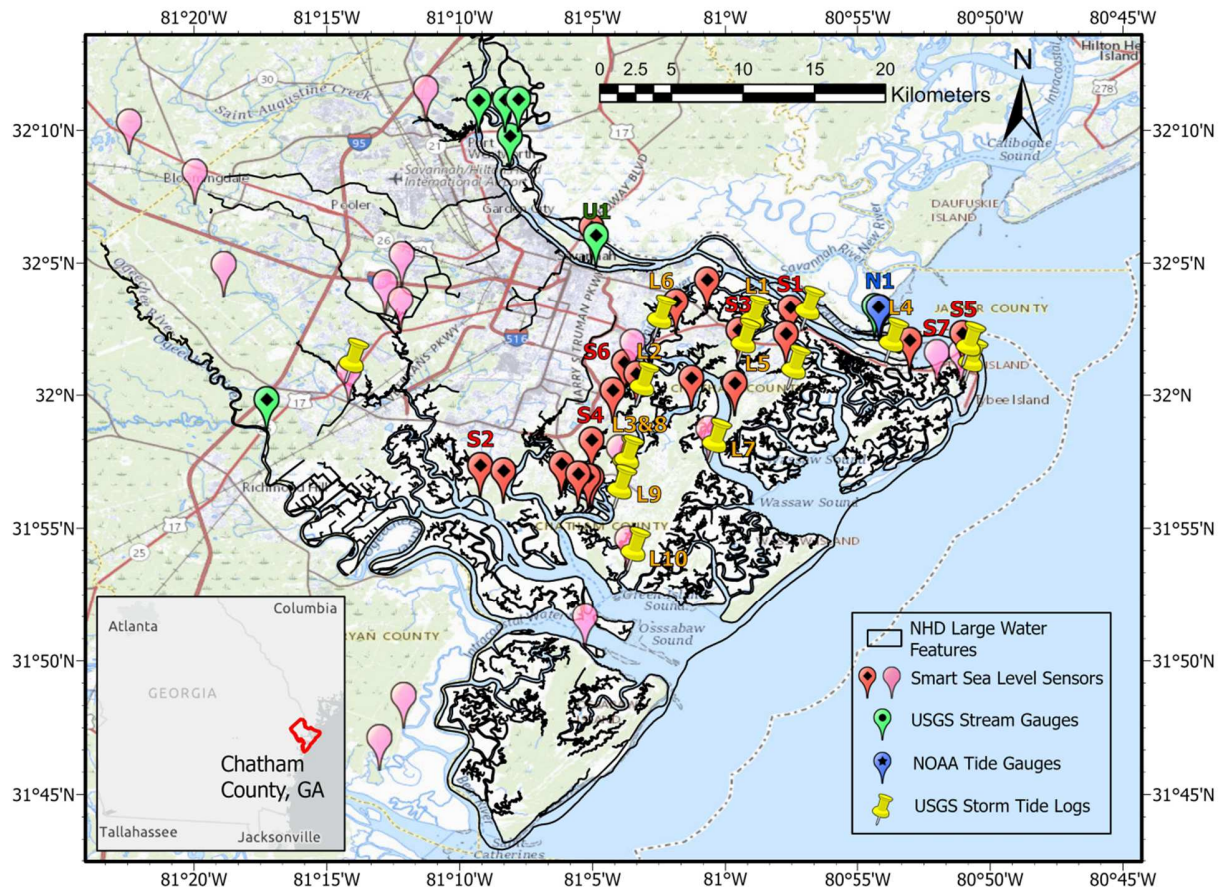
175 for emergency management. We discuss the potential benefits and limitations of the model applications in
176 Section 4. Finally, Section 5 provides a summary and conclusions of the present study.

177

178 **2. Methods**

179 **2.1. Hyper-local water level sensor network: Smart Sea Level Sensors (SSLS)**

180 The SSLS project (<https://www.sealevelsensors.org/>) has installed more than 40 low-cost, power-efficient,
181 Internet of Things (IoT)-enabled water level sensors (red and pink placemarks), across Chatham County,
182 U.S. Georgia, as shown in Fig. 1. The hyper-local sensor network spans a wide range of estuarine
183 channels, prioritizing monitoring of coastal infrastructure that is prone to flooding, such as bridges and
184 marinas. Prior to the SSLS deployments, the NOAA station at Fort Pulaski (blue placemark), the only tide
185 gauge on the entire Georgia coast, provided information on coastal water levels in Chatham County.
186 While USGS also operates multiple monitoring locations, the observation availability remains limited
187 with a small number of stream gauges (green placemarks) located upstream of the estuaries and
188 temporary storm tide loggers (yellow placemarks) to collect water levels during extreme weather events,
189 such as hurricanes. Consequently, the SSLS water level monitoring network provides instantaneous
190 access for public and emergency officials (e.g., Chatham Emergency Management Agency) to identify
191 localized flood threats to coastal communities. The sensor devices are designed to measure the distance to
192 water surface elevation and transmit measurement data into a monitoring server through internet-
193 connected gateways, using ultrasonic sensors and Long Range Wide Area Network (LoRaWAN)
194 technology. As part of the sensor deployments, two validation sensors are placed next to the NOAA tide
195 gauge at Fort Pulaski (blue marker). A comparison of the validation sensors with the NOAA tide gauge
196 indicated less than 0.3 cm differences for two years. Currently, the sensors operate with a power-saving
197 protocol, which involves repeating one measurement cycle of collecting 18 samples for 3 seconds and
198 transmitting the averaged signal every 6 minutes.



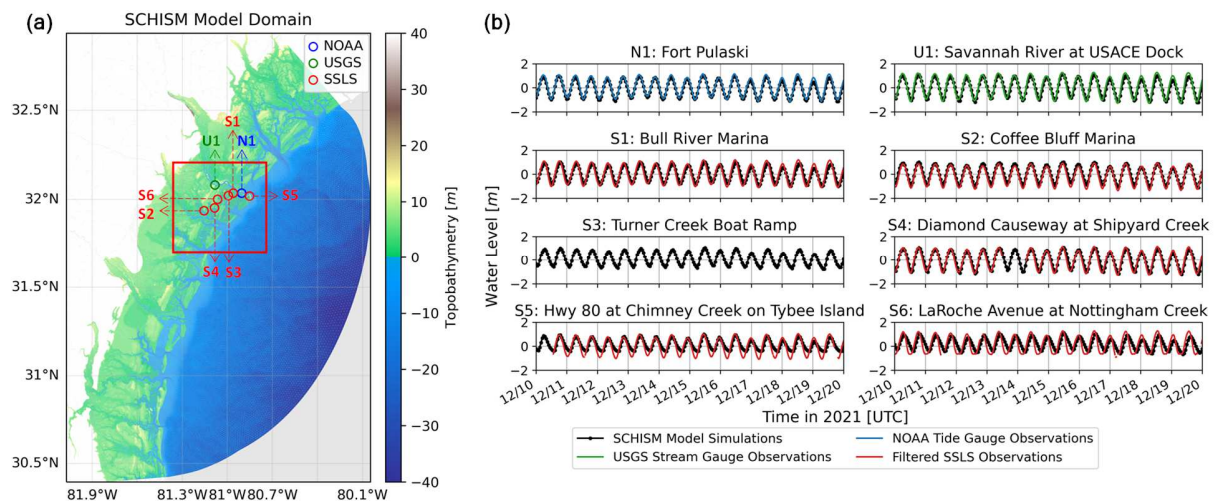
199
200 **Fig. 1** Water level monitoring stations of NOAA, USGS, and SSLS with NHD Large Water Features of Chatham
201 County in GA, USA. Among SSLS locations, the red placemarks indicate those with elevation survey information
202 within NHD Large Water Features. The labeled locations (NOAA: N1, USGS: U1, SSLS: S1-7, and USGS Log: L1-
203 10) will serve as points of reference in our study.

204 **2.2. Water level simulations using a high-resolution coastal-ocean hydrodynamic model**

205 Physics-based model simulations of coastal water levels are performed to establish spatial covariance
206 statistics in the OA procedure. In this study, the Semi-implicit Cross-scale Hydroscience Integrated
207 System Model (SCHISM) (Zhang and Baptista, 2008; Zhang et al., 2016) is implemented to simulate
208 water levels and inundations from the coasts to inland areas along the Georgia coasts. The SCHISM
209 model has been widely used to simulate coastal-ocean circulation processes with an emphasis on three-
210 dimensional baroclinic modes, including storm surge simulations (Zhang et al., 2020; Ye et al., 2020). As
211 shown in Fig. 2a, the model domain covers the entire U.S. Georgia coast with horizontal resolutions
212 ranging from 6 km (around the open boundary) to 3 m (along small rivers and creeks). The
213 topobathymetry for unstructured grid systems is interpolated from the NOAA Continuously Updated
214 Digital Elevation Model (CUDEM; 3 to 100 m resolutions) with local refinements using other sources of
215 NOAA DEM (e.g., Sea Level Rise Viewer DEM; 3 to 5 m resolutions). The model setup integrates inland

217 hydrologic input from the National Water Model (NOAA NWS, 2016). In the model setup, surface waves
 218 are not considered due to their marginal impacts in the study areas, which are characterized by extensive
 219 wetlands along geographically complex channels in estuarine settings (Muñoz et al., 2021). The initial
 220 and boundary conditions are provided by oceanographic datasets from Archiving, Validation and
 221 Interpretation of Satellite Oceanographic (AVISO) and Copernicus Marine Environment Monitoring
 222 Service (CMEMS). A tide model of Finite Element Solution (FES) 2014 is used for the open boundary
 223 condition and tidal potential in momentum equations, including eight major tidal constituents such as K1,
 224 K2, M2, N2, O1, P1, Q1, and S2. The ECMWF Reanalysis 5 (ERA 5) datasets are applied for
 225 atmospheric forcing.

226 The SCHISM model simulations are performed for October 21 to December 30, 2021, including
 227 the model spin-up phase. The simulated water levels for 30 days from November 25 to December 25 (Fig.
 228 A.1) are utilized to calculate spatial covariance statistics in the OA procedure. Fig. 2b compares the
 229 simulated water levels with the observations at the NOAA tide gauge (N1), USGS stream gauge (U1), and
 230 SSLS sensors (S1-6). The comparisons indicate that the SCHISM model setup is capable of simulating
 231 water levels accurately across estuaries, as shown for the multiple locations (N1, U1, S1, S2, and S4) in
 232 Fig. 2b. In addition, our study includes a few locations to assess the capability of the developed OA
 233 approach later in the current study: (S3), where the SSLS sensor was inactive during the simulation
 234 periods, (S5), where discrepancies may exist during low tides due to the model representation of
 235 topobathymetry, and (S6), where a slight phase lag may arise with the model uncertainty.

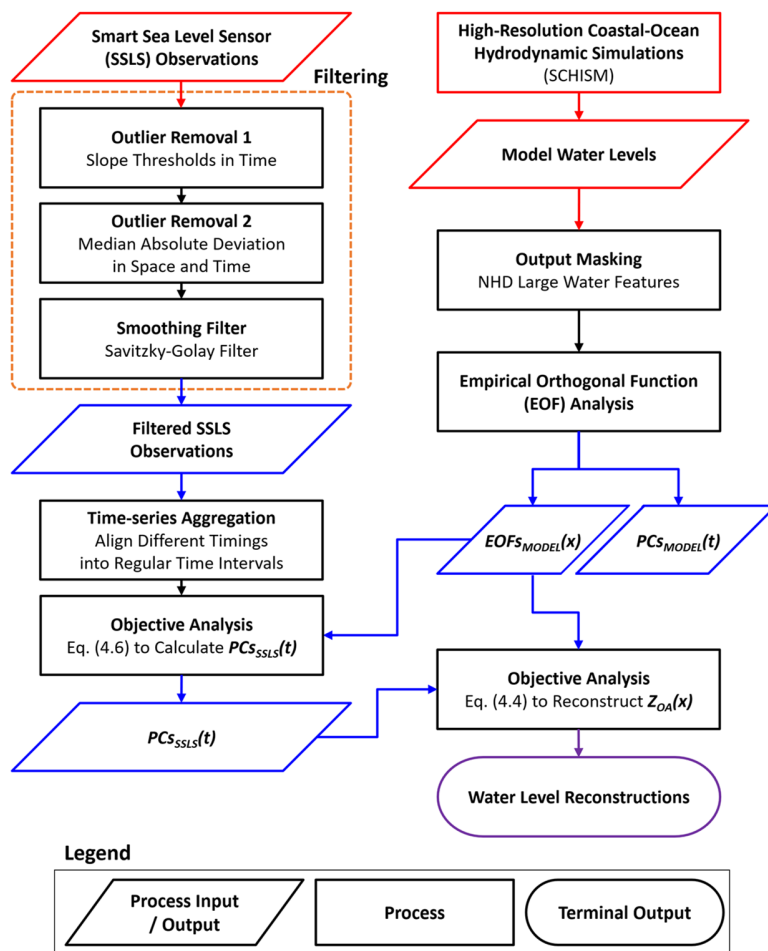


236
 237 **Fig. 2** SCHISM model simulations: (a) model domain and topobathymetry. The red box corresponds to the map
 238 extent in Fig. 1; (b) comparisons of simulated water levels with observations. The headings (N1, U1, and S1-6) on
 239 the titles correspond to the labels of the station locations in Fig. 1. The model evaluations, including error statistics,
 240 are listed in Appendix C.

241

242 2.3. Physics-based empirical modeling of coastal water levels

243 In our study, as outlined in the flowchart in Fig. 3, the reconstruction of water levels is accomplished
 244 through the OA procedure (Chambers et al., 2002) that combines the SSLS observation datasets (Section
 245 2.1) with the spatial covariance statistics of the simulated water levels using the SCHISM model (Section
 246 2.2). Prior to using the observation datasets, a preprocessing procedure is implemented due to different
 247 measurement timings and abnormal signals within water level records. In the simulation results, water
 248 levels in upland areas may experience wet and dry conditions, requiring a masking process for the
 249 numerical model grids to prevent incomplete statistical analysis. The EOF analysis establishes the
 250 statistical covariance structures of the simulated water levels for the masked grids. Using the OA
 251 procedure, the Principal Components time series (PCs) are calculated from the observation datasets
 252 available over a specific period of interest, which are subsequently applied to assimilate a spatial field of
 253 water levels by combining with the established EOFs. The detailed implementations will be described in
 254 the following subsections.



255
 256 **Fig. 3** Flowchart of physics-based empirical modeling of coastal water levels, using SSLS observation datasets.
 257

258 **2.3.1. Preprocessing of SSLS observation datasets**

259 In water level monitoring networks, the operations of sensor devices are often influenced by
260 environmental factors (e.g., animal or human activities) and various instrument conditions (e.g., power
261 supply or network connections) (Spicer et al., 2021). As a result, the SSLS observation datasets may
262 contain abnormal signals, such as sporadic fluctuations, spikes, and occasional outages. To address such
263 issues, a data-processing procedure is applied to filter the water level records, including outlier removals
264 and smoothing, with the following steps:

265 1. *Slope Thresholds in Time*:

266 To identify local outliers in time series data for each sensor, the time rates of change in water
267 levels are calculated from consecutive data points within a specified timeframe to count a portion
268 of excessive or unreasonable changes in water levels. For example, if more than 10 % of
269 neighboring data points within a two-hour timeframe indicate unreasonable changes in water
270 levels (e.g., $> 1 \text{ m/hour}$), the corresponding measurement is deemed unstable and discarded from
271 the analysis. The assessment of the rate of change is highly recommended by Integrated Ocean
272 Observing System (2021).

273 2. *Median Absolute Deviation (MAD) in Space and Time*:

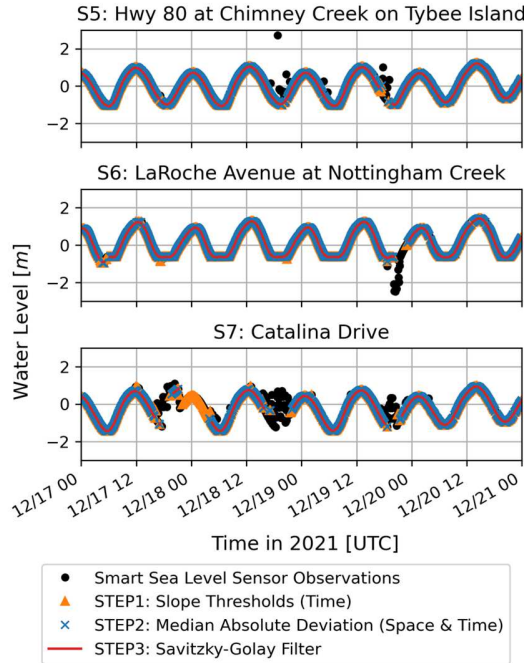
$$\text{MAD} = \text{median}|z_t - \langle z_t \rangle| \quad (1)$$

274 To detect outliers in both space and time, the MAD of the time rate of change in water levels, z_t ,
275 is calculated by using more than five sensor measurements for cross-comparisons in space. Then,
276 if a measurement deviates more than three standard deviations from the calculated MAD, which
277 is equivalent to the Hampel filter (Pearson et al., 2016), it is identified as an outlier and
278 subsequently removed from the analysis. This step is particularly useful when nearby
279 observations are available, as suggested by Integrated Ocean Observing System (2021).

280 3. *Savitzky-Golay Filter*:

281 The Savitzky-Golay filter (Savitzky and Golay, 1964; Gorry, 1990) is applied to smooth time
282 series signals, which involves fitting a piecewise polynomial function to a set of measurements.
283 Specifically, our study uses a third-order polynomial function with a four-hour time window for
284 each measurement.

285 At the beginning of each step, our study excludes measurement points with fewer than four counts within
286 two hours due to the limited representation of water level variations. As an example, Fig. 4 shows the
287 step-by-step preprocessing results for SSLS observation datasets.



288
289 **Fig. 4** Example results of step-by-step preprocessing for SSLS observation datasets: Steps 1 and 2 for outlier
290 removals and Step 3 for smoothing.

291

292 **2.3.2. OA based on spatial covariance statistics**

293 Our study uses the same OA procedure of Chambers et al. (2002) that combines spatial covariance
294 statistics to interpolate water levels from spatially-distributed observation datasets. The OA procedure
295 consists of two main components: the first part applies the EOF analysis to physics-based model
296 simulations of water levels to obtain spatial covariance structures as EOFs, and the second part
297 determines the corresponding PCs for these EOFs based on available observation datasets to reconstruct
298 water levels.

299 The EOF analysis decomposes spatiotemporal variations of water levels into a linear combination
300 of spatial modes (EOFs), multiplied by associated time-varying amplitudes (PCs). Through a singular
301 value decomposition, water levels, $\mathbf{Z} \in \mathbb{R}^{m \times n}$, which is a function of space, $\mathbf{x} \in \mathbb{R}^{m \times 1}$ at m locations,
302 and time, $\mathbf{t} \in \mathbb{R}^{n \times 1}$ for n time steps, can be expressed as:

$$\mathbf{Z}(\mathbf{x}, \mathbf{t}) = \mathbf{U}\Sigma\mathbf{V}^T \quad (2)$$

303 where $\mathbf{U} \in \mathbb{R}^{m \times m}$ is the spatial modes (EOFs), $\Sigma \in \mathbb{R}^{m \times n}$ is the diagonal matrix with the eigenvalues of
304 \mathbf{Z} , and $\mathbf{V} \in \mathbb{R}^{n \times n}$ is the temporal variations of the spatial modes. Hence, Eq. (2) can be rewritten by
305 simply replacing the latter terms with the time-varying amplitudes (PCs), $\alpha(\mathbf{t}) \in \mathbb{R}^{m \times n}$:

$$\alpha(\mathbf{t}) = \Sigma\mathbf{V}^T \quad (3)$$

$$\mathbf{Z}(\mathbf{x}, \mathbf{t}) = \mathbf{U}(\mathbf{x})\alpha(\mathbf{t}) \approx \mathbf{U}_k(\mathbf{x})\alpha_k(\mathbf{t}) \quad (4)$$

306 The columns of \mathbf{U} and rows of $\boldsymbol{\alpha}$ correspond to the individual modes of EOFs and PCs, respectively, and
 307 the subscript, k , denotes the number of the truncated modes. As a result, the EOF analysis enables
 308 reducing the number of modes by selecting a few low-order EOFs and PCs that explain a significant
 309 portion of variances in water levels. In addition, the leading-order EOFs and PCs may characterize
 310 distinct spatial covariance patterns and related temporal variations of water levels.

311 Based on Kaplan et al. (2000), the PCs can be found through a least-squares estimation process
 312 that minimizes the following objective function, S :

$$\min S(\boldsymbol{\alpha}_k) = (\mathbf{H}\mathbf{U}_k\boldsymbol{\alpha}_k - \mathbf{Z}^0)^T \mathbf{R}^{-1} (\mathbf{H}\mathbf{U}_k\boldsymbol{\alpha}_k - \mathbf{Z}^0) + \boldsymbol{\alpha}_k^T \boldsymbol{\Lambda}_k^{-1} \boldsymbol{\alpha}_k \quad (5)$$

$$\boldsymbol{\alpha}_k = (\mathbf{U}_k^T \mathbf{H}^T \mathbf{R}^{-1} \mathbf{H} \mathbf{U}_k + \boldsymbol{\Lambda}_k^{-1})^{-1} \mathbf{U}_k^T \mathbf{H}^T \mathbf{R}^{-1} \mathbf{Z}^0 \quad (6)$$

313 where $\mathbf{Z}^0 \in \mathbb{R}^{p \times n}$ is water level observations at p locations, $\mathbf{H} \in \mathbb{R}^{p \times m}$ is a sampling operator matrix to
 314 consider observation availability, $\mathbf{R} \in \mathbb{R}^{p \times p}$ is the matrix for data error covariances due to instrumental,
 315 sampling, and truncation errors, and $\boldsymbol{\Lambda}_k \in \mathbb{R}^{k \times k}$ is the truncated diagonal matrix with the eigenvalues of
 316 the covariance matrix. As an initial study to apply the OA procedure to assimilate water levels directly
 317 from hyper-local sensor observations, our study implements the simplest approach by Chambers et al.
 318 (2002) where the identity matrix is used for \mathbf{R} and the latter term is omitted as follows:

$$\min S(\boldsymbol{\alpha}_k) = (\mathbf{H}\mathbf{U}_k\boldsymbol{\alpha}_k - \mathbf{Z}^0)^T (\mathbf{H}\mathbf{U}_k\boldsymbol{\alpha}_k - \mathbf{Z}^0) \quad (7)$$

$$\boldsymbol{\alpha}_k = (\mathbf{U}_k^T \mathbf{H}^T \mathbf{H} \mathbf{U}_k)^{-1} \mathbf{U}_k^T \mathbf{H}^T \mathbf{Z}^0 \quad (8)$$

319 Once the PCs are obtained from Eq. (8) for available observation datasets, a spatial field of water levels
 320 can be reconstructed by combining PCs with the EOFs, as shown in Eq. (4).

321 In our study, the water levels simulated by the SCHISM model (over 53,000 grid points) serve as
 322 a basis dataset for the EOF analysis. Prior to performing the EOF analysis, we remove the temporal
 323 means of water levels over the simulation periods and apply the channel boundary based on the USGS
 324 National Hydrography Dataset (NHD) Large Water Features for Chatham County to mask the water level
 325 outputs along the coastal channels, as delineated in Fig. 1. This masking procedure enables us to reduce
 326 the number of grid points involved in matrix computations, with an emphasis on estuarine channels.
 327 Estuarine channels are of primary interest because the majority of SSLS have been deployed to monitor
 328 bridges and marinas. Additionally, we exclude grid points where water levels exhibit little variations and
 329 dry conditions to prevent using incomplete data for the EOF analysis. To align the different timings of the
 330 SSLS measurements in calculating the PCs, the observation datasets are aggregated by averaging them
 331 over a 15-minute interval.

332

333 2.3.3. OA using a Gaussian covariance function

334 The OA procedure commonly employs an analytical covariance function to interpolate a limited set of
335 observations into a spatial field of interest. Based on the Gauss-Markov theorem, the least-square linear
336 estimator can be calculated by

$$\mathbf{Z}^x = \widehat{\mathbf{Z}}^x + \mathbf{C}_{xo} \mathbf{C}_{oo}^{-1} (\mathbf{Z}^o - \widehat{\mathbf{Z}}^o) \quad (9)$$

337 where $\mathbf{Z}^x \in \mathbb{R}^{m \times n}$ is water levels at locations of interest, $\mathbf{C}_{xo} \in \mathbb{R}^{m \times p}$ is the spatial covariances between
338 observations and locations of interest, and $\mathbf{C}_{oo} \in \mathbb{R}^{p \times p}$ is the spatial covariances between all pairs of
339 observations. The $\widehat{\cdot}$ denotes the estimated mean water levels.

340 In the absence of spatial covariance information, it is often assumed that the covariances among
341 the observations themselves, as well as between observations and a spatial field of interest, depend solely
342 on the spatial distance between each pair of locations, regardless of the locations themselves. Among
343 various analytical forms, we use the Barnes Scheme (Barnes, 1964) that adopts a Gaussian function to
344 describe spatial covariances based on distance, which is expressed by:

$$C(x_1, x_2) = f(d) = e^{-(d/L)^2} \quad (10)$$

345 where d and L denote the distance between two locations and the decorrelation scaling parameter,
346 respectively. Consistently with Section 2.3.2, we use the same SSLS measurements that are aggregated
347 over a 15-minute interval. The least-square fitting technique is applied to estimate the linear mean trends
348 of water levels. The decorrelation length scale of 5 km is used based on the preliminary implementation
349 by Tien et al. (2023).

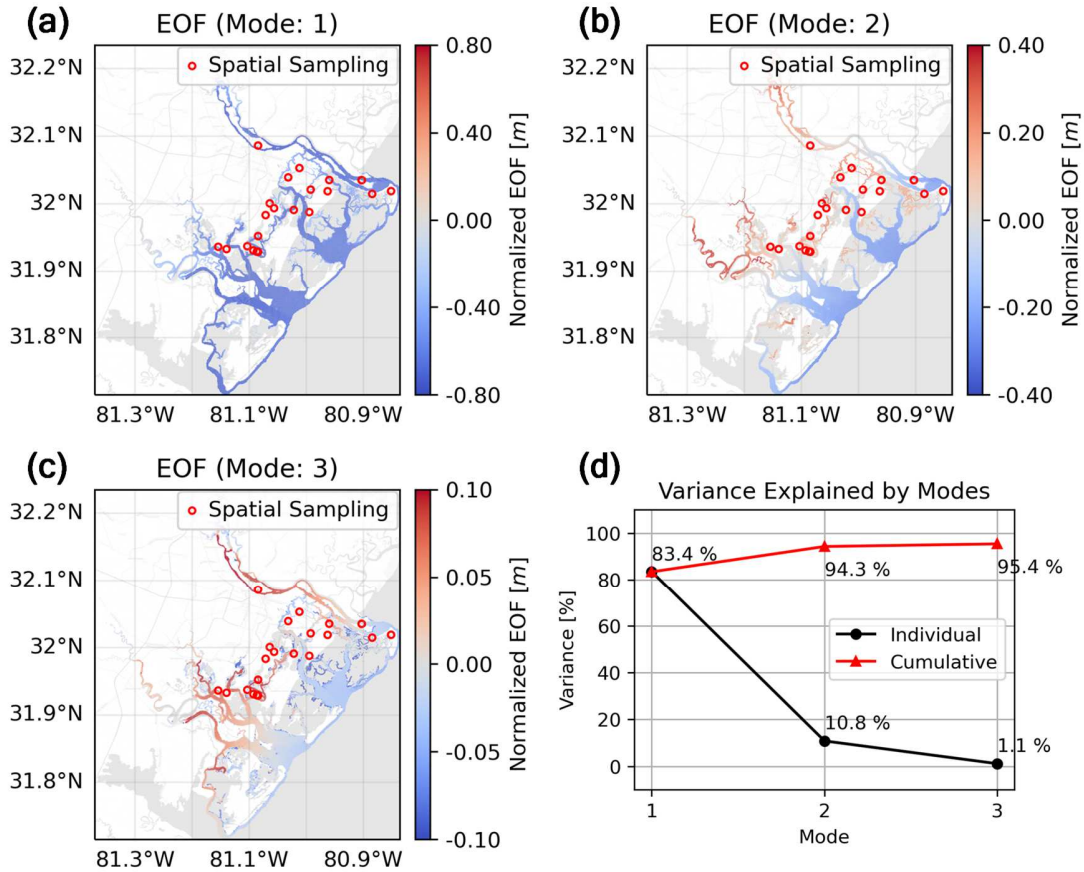
350

351 3. Results and discussion

352 3.1. EOF analysis and sensitivity tests

353 Through a singular value decomposition, the EOFs and PCs are obtained from the SCHISM model
354 simulations of water levels from November 25 to December 25, 2021. Fig. 5 shows the first three spatial
355 modes of the EOFs, along with the associated variance explained by each mode. To facilitate comparison
356 across the different modes, the EOFs and PCs are normalized by multiplying the EOFs with the standard
357 deviations of PCs and dividing the PCs by the standard deviations, respectively. As a result, the
358 normalized EOFs represent the physical magnitudes of the spatial modes while retaining unit standard
359 deviations for the normalized PCs. The lowest EOF mode in Fig. 5a has the strongest signal characterized
360 by uniform water level patterns that can either rise or fall, primarily forced by astronomical tides. Fig. 5b
361 shows the second EOF mode, which exhibits a linear slope pattern in water levels with strong correlations
362 with the distance to open coasts. This linear pattern is likely driven by either flood or ebb tide flowing
363 along the channel landscapes. The third spatial pattern in Fig. 5c is similar to the previous mode but has
364 concentrated signals upstream in the complex channels of the estuaries. As plotted in Fig. 5d, the
365 explained variances significantly decrease as the EOF modes increase, accounting for more than 95 % of

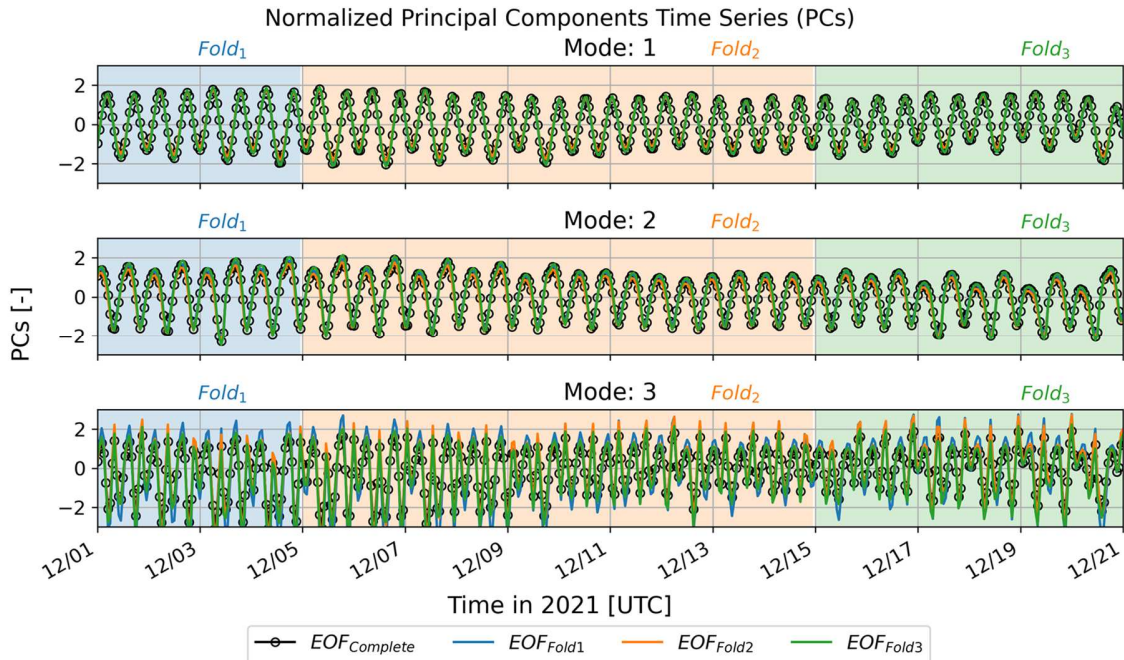
366 the total variances with these three lowest modes. Therefore, our study uses the three dominant EOF
 367 modes for the reconstruction of water levels. The selection of these EOF modes implies that
 368 spatiotemporal variations in water levels result from a combination of rising or falling water levels, their
 369 flooding or receding phase, and adjustments related to upstream dynamics.



370
 371 **Fig. 5** Normalized EOFs and associated variances explained: (a) – (c) three lowest spatial modes of water levels.
 372 The EOFs are normalized with the standard deviations of PCs to indicate physical magnitudes. The red circles
 373 highlight SSLS that are located within the study boundaries and have sensor elevation survey information,
 374 corresponding to the red placemarks in Fig. 1; (d) variances explained by different spatial modes.

375 To assess the stationarity of the EOFs with respect to simulation periods, we implement a 3-fold
 376 test that involves extracting the EOFs from three separate chunks, each spanning 10 days of the
 377 simulation periods. Then, the obtained EOFs are applied to solve Eq. (8) to derive the corresponding PCs
 378 across the simulation periods. However, accurate water level observations will only be available at
 379 locations where SSLS are installed and their elevations are surveyed, which is referred to as spatial
 380 sampling in this study. The effects of spatial sampling due to the limited availability of observations are
 381 taken into consideration in the 3-fold test. Thus, we use the simulated water levels only at 22 SSLS
 382 locations within the study boundaries, which are highlighted with red circles in Fig. 5. As shown in Fig. 6,
 383 the normalized PCs are obtained from the different EOFs based on the three separate chunks of the

384 simulated water level time series. The comparisons of the PCs within each mode show that the leading-
 385 order PCs are not significantly influenced by the selection of water level time series for the EOFs.
 386 However, minor variations are identified in the third PC, particularly around the peaks and troughs of the
 387 PC. Consequently, the EOFs and PCs marginally depend on simulation periods, even when applying the
 388 simulated water levels through spatial sampling for the valid SSLS locations.



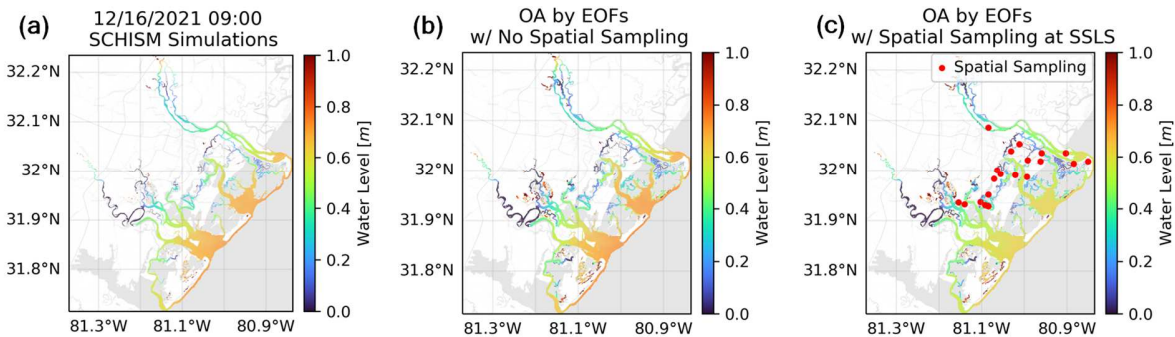
389
 390 **Fig. 6** Normalized PCs derived from the EOF_{Complete} (11/25 – 12/25), EOF_{Fold1} (11/25 – 12/05), EOF_{Fold2} (12/05 –
 391 12/15), and EOF_{Fold3} (12/15 – 12/25). The PCs are calculated from spatial sampling of the simulated water levels at
 392 22 SSLS locations within the study boundaries (red circles in Fig. 5) and normalized by their standard deviations.

393 Regarding the characteristics of the PCs, the first two PCs exhibit similar periodic cycles, which
 394 are highly correlated with astronomical tidal cycles. In addition, the peaks and troughs of the first PC
 395 closely align with the zero-crossings of the second PC, implying out-of-phase differences between the
 396 spatial patterns of the first and second EOF modes. The phase lag corresponds to flood or ebb tidal
 397 currents that reach their maximum at the mean water level between low and high tides. The third PC
 398 shows fluctuations with a higher frequency, suggesting potential adjustments in water levels as water
 399 enters and exits the upstream estuarine channels. These PCs represent the magnitudes, timing, and
 400 interplay between the three dominant EOF modes, assimilating the specific state of estuarine water levels.
 401

402 **3.2. Model verification with SCHISM model simulations**

403 Prior to using the SSLS observation datasets, the simulated water levels from the SCHISM model are first
 404 utilized to reconstruct water levels and identify modeling gaps in the OA procedure. Fig. 7 shows
 405 example plots of water levels at a specific time during flood tides, comparing the SCHISM model

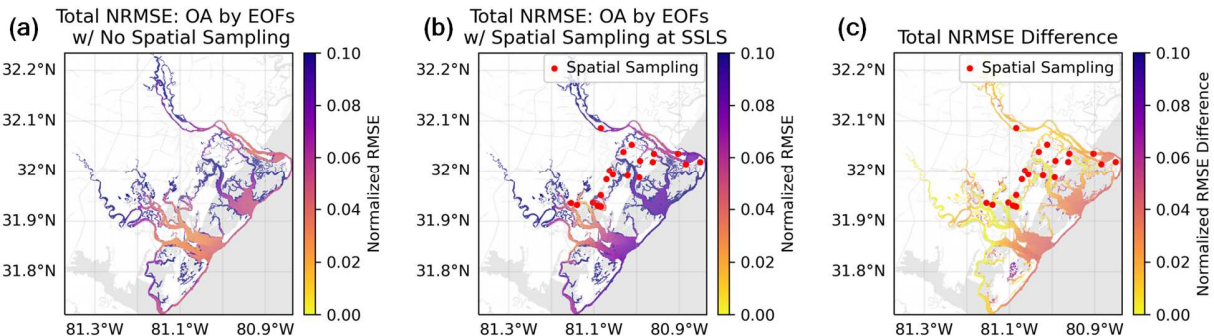
406 simulations (Fig. 7a) with two types of reconstruction: one using all water levels within the study
 407 boundaries (Fig. 7b) and another using water levels only at 22 SSLS locations (Fig. 7c). Despite being
 408 confined to the study boundaries due to the masking procedure, the assimilated water levels are consistent
 409 with the numerical simulation results. However, the spatial sampling leads to discrepancies in the
 410 assimilation of water levels, particularly in the immediate coasts due to the limited sampling of water
 411 level data in these areas.



412
 413 **Fig. 7** Example plots of water levels at 12/16/2021 09:00 UTC during flood tide: (a) SCHISM model simulations; (b)
 414 EOFs-based reconstruction with all the simulated water levels shown in (a); (c) EOFs-based reconstruction with
 415 spatial sampling at 22 SSLS locations within the study boundaries (red circles).

416 Error statistics are calculated for the 30-day simulation periods, employing multiple evaluation
 417 metrics that are described in Appendix B. The SCHISM model simulations are regarded as a ground truth
 418 as the simulated water levels are currently used to compute the PCs using Eq. (8). Consequently, the
 419 evaluation metrics provide a means to assess the reconstruction capabilities of water levels, in comparison
 420 with an ideal EOFs-based OA procedure without errors. Fig. 8 shows the normalized root-mean-square
 421 errors (NRMSE) as defined in Eq. (B.2), using all information within the study boundaries (Fig. 8a) and
 422 using spatial sampling limited to 22 SSLS locations (Fig. 8b). The first NRMSE in Fig. 8a represents
 423 truncation errors resulting from using the three leading spatial modes of water levels, which remain below
 424 0.05. However, it should be noted that some upstream channels have relatively higher NRMSE values,
 425 indicating limitations in capturing the dynamics only with a few EOFs due to complex interactions
 426 between water and estuarine landscapes. The second NRMSE in Fig. 8b corresponds to spatial sampling
 427 errors arising from the limited availability of observations, in addition to the truncation errors. The
 428 NRMSE values increase up to 0.1 for distant areas from the valid SSLS locations, particularly in
 429 proximity to the immediate coasts. The difference between the two NRMSEs, as shown in Fig. 8c,
 430 indicates the portion of the reconstruction errors originating solely from spatial sampling. The NRMSE
 431 differences are generally less than 0.04 but become more pronounced towards the outer study boundaries.
 432 This is because the majority of the SSLS deployments are centered around urban areas where coastal

433 infrastructure is located. A similar discrepancy is also captured during flood tide, as observed in Fig. 7b
 434 and Fig. 7c.



435
 436 **Fig. 8** NRMSE calculations based on the SCHISM model simulations as a ground truth: EOFs-based reconstructions
 437 (a) with the simulated water levels and (b) with spatial sampling at 22 SSLS locations within the study boundaries
 438 (red circles); (c) NRMSE difference between (a) and (b).

439 Table 2 summarizes the median and quantile values of other evaluation metrics that are defined in
 440 Appendix B. These metrics are applied to more than 53,000 SCHISM grid points within the study
 441 boundaries. Since the grid points are distributed unevenly depending on channels, the median and quantile
 442 values of the error statistics are selected to represent the relative trends in accuracy. The overall RMSE
 443 slightly increases due to the spatial sampling for 22 SSLS locations, as identified particularly for the
 444 lower quantile value from 0.039 m to 0.052 m. On the other hand, the MBE, R, and NSE show minor
 445 changes within acceptable ranges.

446 **Table 2**
 447 Error statistics of water level reconstructions using the simulated water levels from the SCHISM model as a ground
 448 truth. For comparison, the median and quantile values are calculated from more than 53,000 SCHISM grid points.

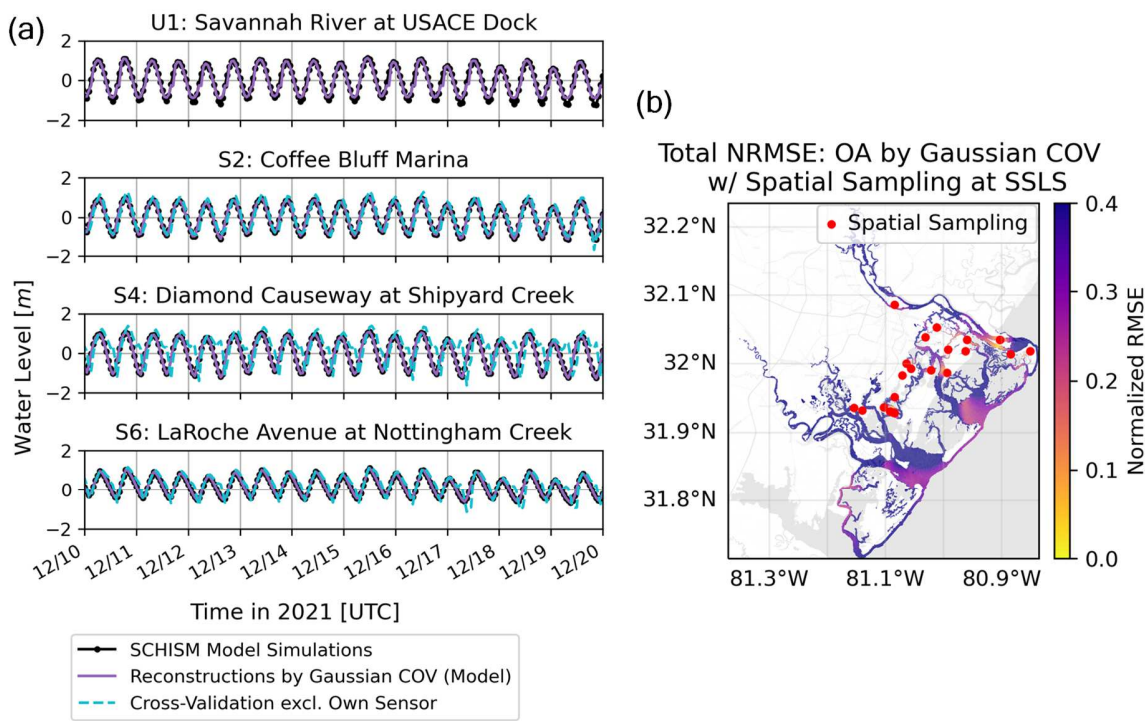
Water level availability	Spatial covariance	RMSE [m]			MBE [m]			R [-]			NSE [-]		
		25%	50%	75%	25%	50%	75%	25%	50%	75%	25%	50%	75%
All locations	EOFs	0.037	0.055	0.088	0.000	0.000	0.000	0.982	0.994	0.999	0.963	0.988	0.997
22 SSLS locations	EOFs	0.050	0.064	0.083	0.000	0.000	0.000	0.978	0.993	0.997	0.956	0.987	0.994
	Gaussian	0.209	0.383	0.723	-0.223	-0.046	0.038	0.688	0.882	0.965	-1.426	0.551	0.899

* RMSE: root-mean-square errors, MBE: mean bias errors, R: correlation coefficients, and NSE: Nash-Sutcliffe efficiency.

449 Both Fig. 8 and Table 2 suggest that the current EOFs-based OA procedure has more prominent
 450 errors due to the leading-order truncations compared to those attributed to the limited availability of
 451 observations. Although adding higher-order EOF modes may lead to an improved representation of local
 452 dynamics, the corresponding observations in those local regions should be followed to accurately estimate
 453 the contributions through the PCs. With the error statistics, the accuracy and confidence maps can be
 454 generated to guide the practical applications of the EOFs-based OA procedure. In addition, the evaluation

455 metrics can serve as a useful indicator to identify potential locations for additional sensor deployments to
 456 enhance the reconstruction capabilities of the OA procedure (Tien et al., 2023).

457 Based on a Gaussian covariance function, we perform similar reconstructions using the simulated
 458 water levels at 22 SSLS locations. As shown in Fig. 9a, the OA approach reproduces the simulated water
 459 levels for the utilized SSLS locations as expected. However, when excluding the sensor's own location
 460 for cross-validation (light blue dashed lines), the reconstructed water levels fluctuate with offsets and
 461 phase lags (S4 and S6). Similarly, as demonstrated in Fig. 9b, the NRMSE rapidly exceeds 0.1 for areas
 462 away from the valid SSLS locations. Table 2 also includes the error statistics of water level
 463 reconstructions using a Gaussian covariance function. Compared to the EOFs-based OA procedure,
 464 however, all evaluation metrics indicate inadequate performance, particularly with noticeable variations
 465 in RMSE (upper quantile value of 0.723 m) and NSE (lower quantile value less than zero).



466
 467 **Fig. 9** OA results based on a Gaussian covariance function: (a) reconstructions of water levels at SSLS locations.
 468 The light blue dashed lines represent reconstructions with the sensor's own location excluded; (b) a spatial map of
 469 NRMSE.

470 The analytical OA procedure could be improved by adjusting the decorrelation scaling parameter
 471 or by incorporating a more refined analytical function to characterize spatial covariances (Verri et al.,
 472 2017). However, the large reconstruction errors can be attributed to the simplified representation of a
 473 Gaussian covariance function without physical information (Rong and San Liang, 2022), such as
 474 hydrologic connections. Additionally, using a single value for the decorrelation length scale may not be
 475 appropriate for representing the variable density of SSLS deployments across estuaries. Since the

476 analytical OA procedure fails to accurately represent complex patterns of water levels in estuaries, we
477 exclude its further applications in this study.

478

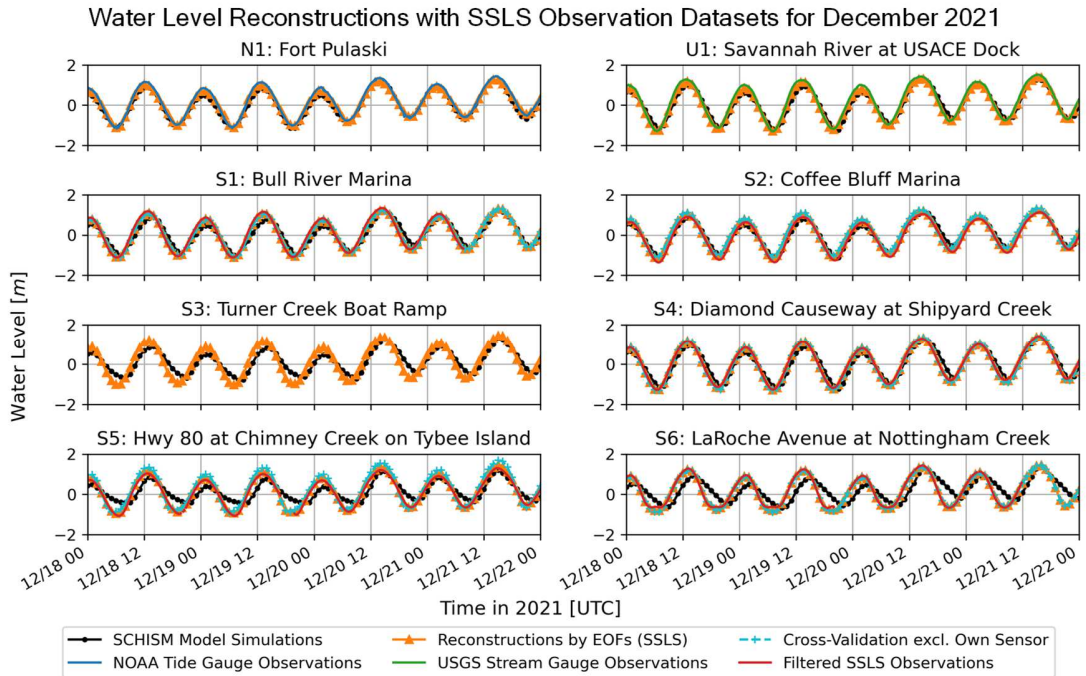
479 **3.3. Model applications with SSLS observations**

480 **3.3.1. Validation for basis simulation periods**

481 Using the SSLS observation datasets, we apply the OA procedure integrating the established structures of
482 spatial covariance to assimilate water levels. It is important to note that the availability of SSLS
483 observations depends on the operational status of individual sensors at the time of monitoring.

484 Throughout the same simulation periods, a total of 12 SSLS devices were active although some sensors
485 were sporadically inoperative. Fig. 10 shows comparisons of the reconstructed water levels (orange lines)
486 with the SCHISM model simulations (black lines) and the available observation datasets (blue line for a
487 NOAA tide gauge, green line for a USGS stream gauge, and red lines for SSLS observations).

488 Additionally, cross-validation cases are included to evaluate the reconstruction sensitivity and robustness
489 when excluding the corresponding SSLS measurements (light blue dashed line). The EOFs-based OA
490 procedure enables providing access to water levels along estuarine channels even in the absence of direct
491 observations, as demonstrated throughout the S3 periods and later portions of S1 and S6 (discontinued
492 SSLS measurements after 12:00 on December 21). This capability to fill in missing measurements is
493 further supported by the effective reconstructions of water levels without the SSLS's own observations. In
494 cases where discrepancies exist between the SSLS observations and physics-based model simulations (S5
495 and S6), the reconstructed water levels closely track the measurements of the SSLS monitoring network.
496 By minimizing error variances directly using actual SSLS observations, the EOFs-based OA procedure
497 realistically determines the weights of spatial covariance structures, identifying the most probable spatial
498 state of water levels. Therefore, the EOFs-based OA procedure has the advantage of leveraging empirical
499 observations that closely approximate the true conditions of water levels.

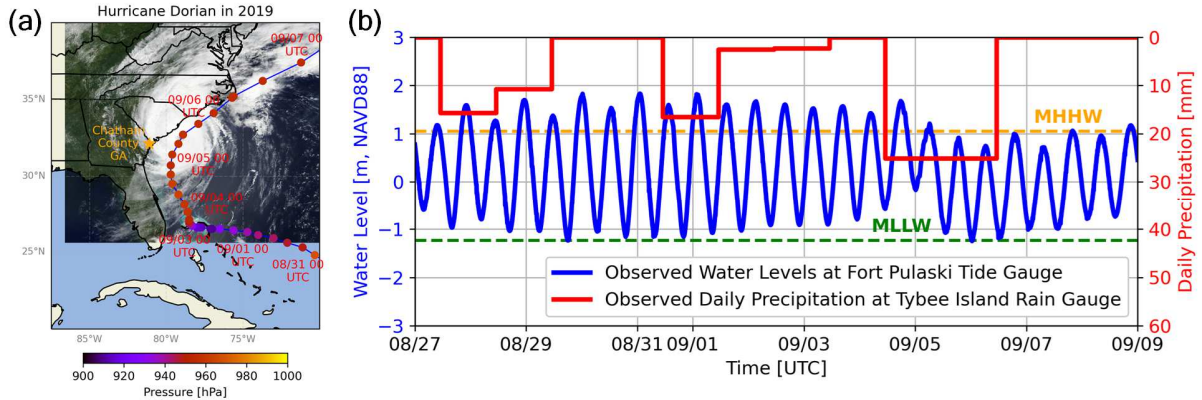


500
501 **Fig. 10** Water level reconstructions using SSLS observation datasets for the basis simulation periods. The cross-
502 validation cases (light blue dashed lines) correspond to excluding the sensor's own measurements for
503 reconstructions. The model evaluations, including error statistics, are listed in Appendix C.

504

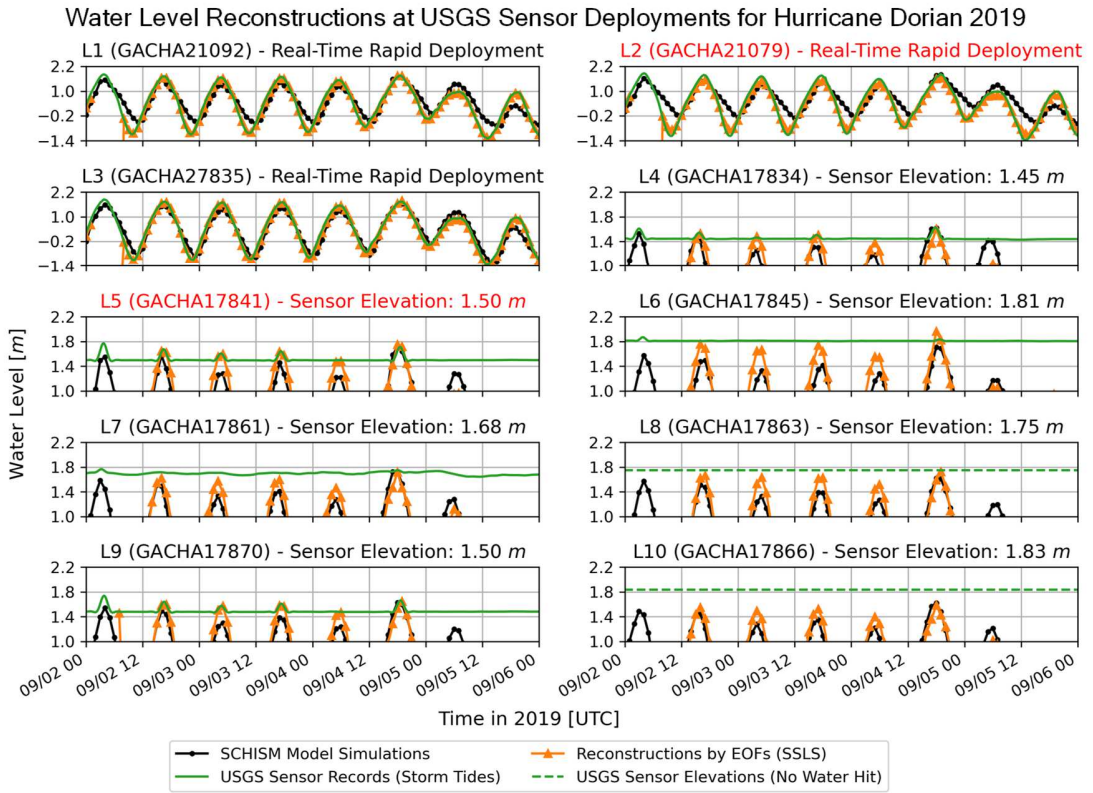
505 **3.3.2. Application for Hurricane Dorian in 2019**

506 Based on the spatial covariance information derived in Section 3.1, the assimilation of water levels is
507 performed for Hurricane Dorian in 2019 to evaluate the capabilities of the OA procedure. Since the SSLS
508 deployments in 2019, Hurricane Dorian has been identified as the most impactful hurricane that closely
509 approached the Georgia coasts. As shown in Fig. 11, although the occurrence of the storm surge on
510 September 05 did not coincide with the astronomical tidal peaks, the hurricane generated wind gusts of
511 approximately 95 *km/hour* and induced a storm surge exceeding 1 *m* along the Georgia coasts (Avila et al.,
512 2020). Consequently, the combined effects of the storm surge and prevailing winds may cause variability
513 in water levels across the estuaries. The SSLS observation datasets are applied for the assimilation of
514 water levels during Hurricane Dorian. 17 SSLS devices measured hyper-local water levels when the
515 hurricane moved along the U.S. East Coast (September 02 to 06). In addition, numerical simulations are
516 independently conducted using the SCHISM model for 30 days from August 20 to September 19, 2019.
517 The model setup is the same as described in Section 2.2, except for using more refined atmospheric
518 forcing obtained from the NOAA High-Resolution Rapid Refresh (HRRR) datasets.



519
 520 **Fig. 11** Hurricane Dorian in September 2019: (a) hurricane track with intensity and (b) water levels (blue) at the
 521 NOAA Fort Pulaski tide gauge and daily precipitation (red) at the local rain gauge. Satellite image credit: MODIS
 522 Land Rapid Response Team and NASA GSFC (2019).

523 For comparison, we employ the USGS storm tide records (yellow placemarks in Fig. 1) that were
 524 collected during Hurricane Dorian, which include additional locations beyond the active SSLS positions.
 525 In Fig. 12, the assimilated water levels (orange lines) are compared with the USGS storm tide records
 526 (green lines), as well as the SCHISM model simulations (black lines). The USGS storm tide sensors
 527 consist of two different types: radar-based rapid deployment gauges that continuously measure water
 528 levels (L1-3) and pressure-based storm tide gauges that read water levels exceeding the sensor elevation
 529 thresholds (L4-10). The assimilated water levels for the L1 to L3 locations show a good agreement with
 530 the storm tidal cycles recorded by radar-based USGS sensors. Moreover, at the L4 to L10 locations, the
 531 peaks of assimilated water levels closely capture the instances where water levels temporarily exceed the
 532 sensor elevations, except for a slight overestimation at the L6 location. At the L8 and L10 locations where
 533 no water hit the sensors, both the assimilated and simulated water levels consistently remain below the
 534 sensor elevation thresholds.



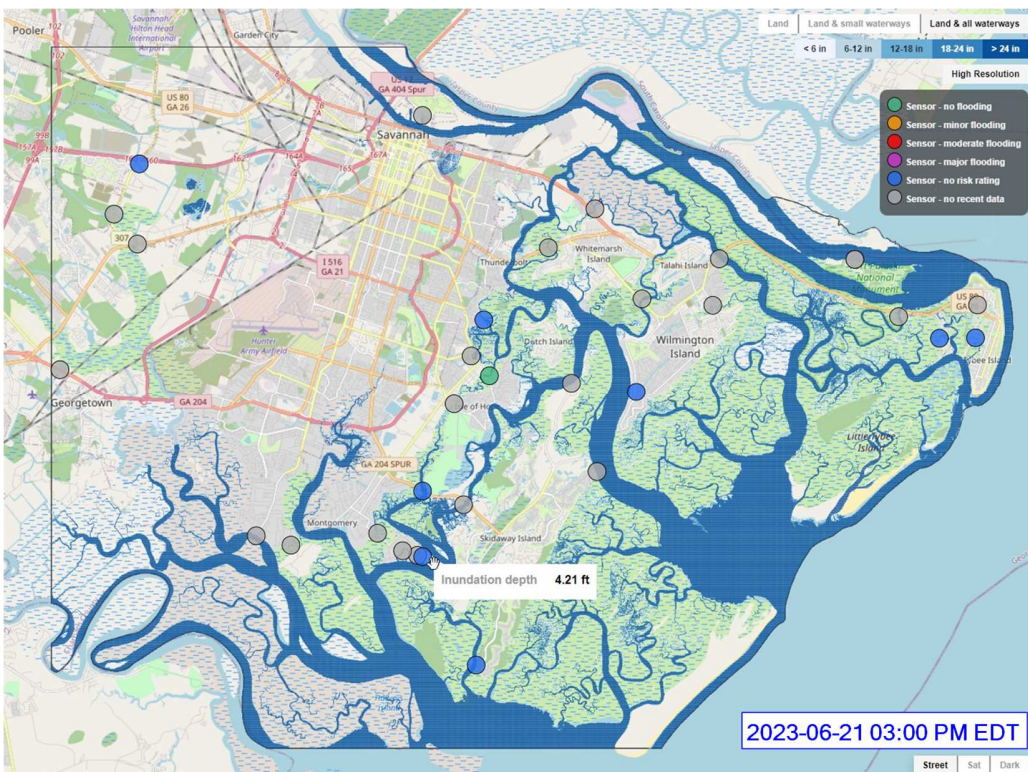
535
536
537
538
539
540

Fig. 12 Comparison of water levels at USGS storm tide monitoring locations during Hurricane Dorian in 2019. The recorded data from radar-based sensors (L1-3) have continuous measurements while those from pressure-based sensors (L4-10) provide actual readings only when water levels reach the specific elevation thresholds. The headings (L1-10) on the titles correspond to the labels in Fig. 1. The titles highlighted in red indicate the locations where the SSLS measurements are available nearby.

541 The application of the EOFs-based OA procedure reveals several limitations. During the initial
542 comparison periods (09/02 02:00 to 08:00), no assimilation outputs are available due to the complete
543 unavailability of observation datasets from the SSLS monitoring network. Although water levels can be
544 directly assimilated based on at least one SSLS observation, there is currently a lack of information
545 regarding the minimum number of SSLS observations required at different locations to ensure accuracy.
546 In addition, it should be noted that the assimilated water levels are spatially confined to coastal channels
547 and temporally limited to historical and real-time applications, in comparison with the simulation results.
548 Nevertheless, the physics-based empirical modeling of water levels demonstrates its capability to
549 reconstruct water levels along coastal channels in an acceptable manner, even for extreme weather events
550 where various dynamic factors can influence water levels.

551

552 **3.3.3. Real-time application in a web-based portal for emergency management**
 553 By adopting spatial covariance statistics derived from numerical simulations, the physics-based empirical
 554 modeling approach maintains computational efficiency, which enables real-time assimilation of coastal
 555 water levels and subsequent applications for monitoring coastal inundation. As demonstrated in Fig. 13,
 556 real-time visualizations of inundation depths are implemented within a pilot web-based portal for the
 557 Chatham Emergency Management Agency (CEMA), along with simultaneous access to SSLS
 558 observations. The operational platform uses the most recent 15-minute SSLS observations to calculate the
 559 real-time state of water levels, leveraging the established spatial covariance structures. Then, the
 560 corresponding inundation depths, which are of primary interest to public and emergency officials, are
 561 determined by subtracting the topobathymetry data. In addition, the NRMSE statistics (Fig. 8) are
 562 employed to extract areas with sufficient accuracy (e.g., NRMSE < 0.3). As a result, the spatial maps of
 563 water levels can provide information even for inactive sensor locations (gray circles) and areas beyond
 564 the immediate vicinity of sensor installations (in between circles). The expanded spatial coverages allow
 565 community officials to promptly identify potential flood threats and take appropriate actions for effective
 566 emergency management. Moreover, the increased access to real-time water levels contributes to
 567 enhancing situational awareness of floods in coastal communities.



568 **Fig. 13** Real-time application in a pilot web-based portal for the Chatham Emergency Management Agency in U.S.
 569 Georgia. The blue contour overlay depicts inundation depths, which represent water heights above topographic
 570 elevations. The circles with color indicate active SSLS locations at the time of monitoring.
 571

572

573 **4. Discussion**

574 Our study demonstrates the implementation of the EOFs-based OA procedure to enhance hyper-local
575 water level monitoring in complex estuarine settings, informed by geospatial statistics from physics-based
576 numerical model simulations. The EOF analysis, which is applied to simulated water levels, enables the
577 extraction of water level patterns that represent the complex dynamics of water flows and interactions
578 within estuarine channel networks, as well as the substantial reduction of the output dimensionality into a
579 few principal modes. Once spatial covariance structures are established through the EOF analysis, the
580 integration with IoT-enabled sensor observations of water levels facilitates the generation of either a
581 retrospective or real-time map of assimilated water levels (Fig. 13).

582 The enhanced access to hyper-local water level conditions can benefit community officials by
583 providing reliable estimates of water levels beyond active sensor locations (e.g., blue or green circles in
584 Fig. 13), extending to coastal infrastructure with neither sensor installation nor observation (e.g., S3 in
585 Fig. 10 and gray circles in Fig. 13). By using a real-time map of assimilated water levels during uncertain
586 flood situations, for example, public and emergency management officials can anticipate potential
587 overtopping at different bridges and flooding at piers, docks, and boat ramps. Given the limited
588 adaptability of coastal infrastructure in response to rising sea levels, the continuous monitoring of
589 increased flood risks to coastal infrastructure is significant for coastal communities to develop strategies
590 for long-term flood resilience (Habel et al., 2020; Son et al., 2023).

591 While coastal-ocean hydrodynamic models are capable of effectively simulating water levels (Fig.
592 2), the operation of forecasting systems demands substantial computational resources (Kerr et al., 2013;
593 Bilskie et al., 2020), which may be prohibitive for coastal communities with limited access. Nonetheless,
594 the EOFs-based OA procedure can efficiently provide timely updates on real-time water level information.
595 This efficiency and utility are particularly evident during non-extreme flood events, when the
596 effectiveness of applying a coastal-ocean hydrodynamic model is in question. Moreover, it is important to
597 note that even calibrated numerical model simulations retain inherent uncertainties that persist throughout
598 the simulation periods (e.g., S5 and S6 in Fig. 2) (Muñoz et al., 2022). The empirical modeling
599 component of the EOFs-based OA procedure facilitates not only the emulation of available water level
600 observations (e.g., S5 and S6 in Fig. 10) but also the generation of the most likely spatial state
601 representation across estuaries. Furthermore, the differences between assimilated water levels and
602 operational predictions produced by coastal-ocean hydrodynamic models can be integrated to update the
603 initial or forcing conditions within operational forecasting system through additional assimilation steps
604 (e.g., Madsen et al., 2015; Asher et al., 2019), which can consistently reduce uncertainties in water level
605 predictions.

606 The geospatial evaluations of modeling errors (Fig. 8) play an important role in informing model
607 accuracy and confidence across various areas and subsequently optimizing sensor deployments to
608 constrain modeling errors. If these modeling errors are linked to a specific EOF mode, its prominent
609 amplitudes and nodal structures can provide valuable insights into ideal locations for additional sensor
610 deployments to ensure high signal-to-noise ratios. In the current modeling framework, which lacks
611 weighting for different sensor locations (Eqs. (5) and (7)), adding a few sensor locations into the existing
612 arrangement is less likely to reduce modeling errors noticeably. Therefore, rigorous optimization
613 techniques, such as the Monte Carlo simulation, can provide a systematic approach to configuring optimal
614 sensor deployments with different weighting. Furthermore, optimizing sensor deployments needs to take
615 into consideration various practical factors. For instance, although the immediate coastal regions currently
616 exhibit higher spatial sampling errors (Fig. 8c), most of these areas consist of extensive wetlands, which
617 are little relevant to real-time flood monitoring. Additionally, other practical factors, such as social
618 vulnerability priorities and potential flood impacts due to critical infrastructure failures, should be
619 incorporated into the optimization process to maximize the marginal benefits of additional sensor
620 deployments. For the SSLS monitoring network, Tien et al. (2023) applied a multi-objective optimization
621 approach based on these practical criteria, in addition to the modeling errors of the OA technique.

622 There are several limitations identified in the applications of the EOFs-based OA procedure,
623 which will be discussed in the subsections below.

625 **4.1. Limitations**

626 **4.1.1. Hyper-local water level sensor observations**

627 The EOFs-based OA procedure is inherently constrained by the limitations of hyper-local water level
628 sensor observations in monitoring networks. Currently, the community-driven monitoring networks
629 (Table 1) are designed to augment water level monitoring, primarily for high tides, storm surges, and
630 rising sea levels. To address the sparse availability of observations from the NOAA tide gauges and
631 USGS stream gauges in coastal communities, these monitoring networks deploy cost-effective, power-
632 efficient sensor instruments, which are engineered to measure water levels at an operational cycle of 2- to
633 6-minute intervals (Observation Cycle column in Table 1), similar to the NOAA (6-minute intervals) and
634 USGS (5-minute intervals) gauges. However, due to these observation cycles, the current sensor
635 observations and their data-processing (e.g., Fig. 4) do not adequately capture water level fluctuations
636 caused by certain flood drivers occurring at shorter timescales, including those associated with short and
637 infragravity waves. To accurately resolve shorter-period water level fluctuations in observations and
638 utilize observation datasets for reconstruction, it is necessary to implement a dedicated observation

639 campaign and specialized operation protocols (e.g., Sweet et al., 2015), which differ from those of the
640 community-driven monitoring networks.

641

642 **4.1.2. EOFs: spatial covariance statistics**

643 Our study uses a month-long dataset of simulated water levels for the EOF analysis to derive spatial
644 covariance statistics (Fig. 5). The stationarity of the EOFs is evaluated with a 3-fold test, which compares
645 the time-varying amplitudes of the EOFs computed from the different chunks of the simulation time
646 series (Fig. 6). In our study, the EOFs-based OA procedure primarily aims to assimilate real-time water
647 levels for extensive flood monitoring, including both nuisance flooding (e.g., high tides with rising sea
648 levels) (Moftakhari et al., 2018; Li et al., 2021) and extreme flooding (e.g., storm surges). Consequently,
649 the EOF and stationarity analysis focuses on identifying robust spatial covariance statistics from water
650 level simulations over a longer period than typical flood timescales. This approach allows capturing
651 quasi-static responses of water levels that predominantly balance in estuarine systems by forcings and
652 facilitating real-time assimilation of water levels, rather than flood prediction under anticipated metocean
653 conditions (e.g., Rohmer et al., 2023 using a surrogate model with multivariate statistical analysis). While
654 our study can reproduce water level variations during a moderate storm surge event (e.g., Fig. 12 for
655 Hurricane Dorian in 2019) using the established EOFs, the stationarity of the EOFs may not hold under
656 different climates, seasons, and weather conditions. Therefore, future research should prioritize exploring
657 the applicable ranges of the EOFs-based OA procedure in these diverse conditions. In particular, it is
658 important to further understand the limitations of the modeling approach during various hurricane and
659 hydrologic runoff events, which are recognized as extreme flood drivers for coastal communities. Then,
660 researchers can identify specific conditions under which the modeling approach may perform less
661 accurately and work towards improving its robustness in such scenarios. As operational forecasts of
662 coastal-ocean hydrodynamic models become increasingly accessible across different climates, seasons,
663 and weather conditions, future research should aim to provide a more comprehensive assessment of
664 stationarity and improve representative spatial covariance statistics of water levels along estuarine
665 channels.

666 Prior to the EOF analysis, the masking process is applied to prevent incomplete statistical
667 analysis, which results in water level assimilations that are spatially confined to coastal channels. To
668 address the spatial confinement, additional mapping techniques, such as downscaling extrapolations (e.g.,
669 Rucker et al., 2021), can be integrated to extend assimilated water levels from coastal channels into inland
670 regions. Moreover, by imposing assimilated water levels as spatiotemporal boundary conditions, coastal-
671 urban flood models can simulate subsequent flooding within urban systems (e.g., Karamouz et al., 2017;

672 Son et al., 2023). These integrations can enhance spatial coverages of assimilated water levels, thus
673 facilitating more comprehensive and efficient flood predictions beyond coastal channels.

674

675 **5. Summary and conclusions**

676 With a growing number of water level monitoring networks, coastal communities have more access to
677 real-time water level information at sensor deployment locations. These hyper-local water level
678 observations enable public and emergency management officials to identify and assess localized flood
679 threats to coastal infrastructure, particularly in areas that have limited capacity to adapt to sea level rise.
680 In line with these community-driven efforts, our study develops a physics-based empirical modeling
681 approach that can efficiently assimilate estuarine water levels from hyper-local sensor observations to
682 enhance water level monitoring capabilities.

683 Our approach uses the OA procedure that combines hyper-local sensor observations with spatial
684 covariance statistics of water levels in coastal regions. Prior to the OA procedure, outlier removal and
685 smoothing techniques are implemented to mitigate the impacts of anomalous signals, including occasional
686 spikes and fluctuations, in the hyper-local sensor observations (Fig. 4). The representative patterns for
687 spatial covariances are established through the EOF analysis on numerical simulations using the high-
688 resolution coastal-ocean hydrodynamic model, SCHISM. The significant spatiotemporal variations in
689 water levels are decomposed into a combination of rising or falling movements, transitional phases
690 between them, and adjustments in the upstream channel (Fig. 5), all of which interact within the complex
691 estuarine settings. Through the 3-fold cross-validations, we demonstrate minor sensitivity to the selection
692 of basis simulation periods for extracting the spatial mode patterns (Fig. 6). In addition, we investigate the
693 assimilation modeling errors associated with the leading-order truncations of the spatial mode patterns
694 and the limited availability of the SSLS observations. Although the truncation errors tend to be larger than
695 the spatial sampling errors, the overall modeling errors remain within acceptable ranges (Fig. 8). When
696 compared to the common OA procedure using a Gaussian covariance function, the EOFs-based OA
697 procedure shows enhanced performance and robustness in assimilating water levels. The improvement is
698 attributed to the inherent limitations of simplified distance-based analytical functions that inadequately
699 capture the complex dynamics of estuaries, including hydrologic connections. Using the actual SSLS
700 observations, the applications of the EOFs-based OA procedure successfully reproduce the temporal
701 patterns and peak magnitudes of water levels along coastal channels for both the basis simulation periods
702 (Fig. 10) and Hurricane Dorian (Fig. 12), demonstrating the capability of our approach to leverage the
703 empirical observations in combination with physics-based statistical information. The assimilation results
704 for Hurricane Dorian show promise in capturing water level states during unusual weather events.

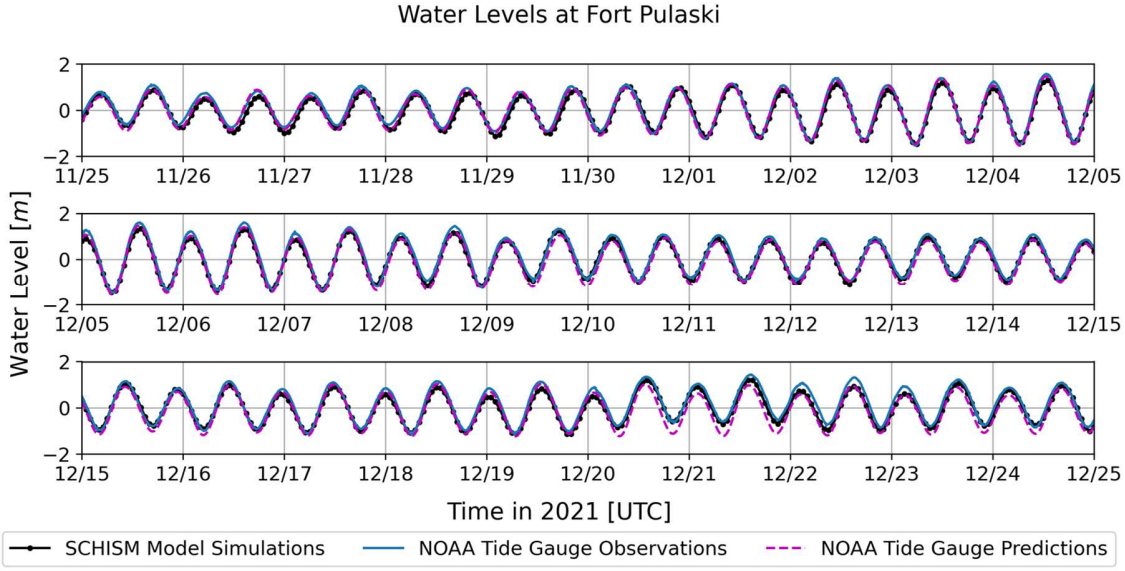
705 However, further validations are necessary to evaluate the extensibility of the modeling approach for
706 different storms with large forcing signals and significant impacts on water level variations.

707 With the established spatial covariance statistics, the real-time assimilation of water levels (Fig.
708 13) can provide community officials with a broader understanding of hyper-local water level conditions,
709 including temporarily inactive monitoring locations and areas that are not covered by sensors. Thus, the
710 assimilation data can serve as a supplementary tool for consistent monitoring of immediate flood risks to
711 coastal infrastructure systems, such as bridges and marinas. Ultimately, coastal communities can make
712 advanced use of water level monitoring networks by integrating the real-time assimilation framework to
713 develop adaptive strategies for flood resilience planning in response to rising sea levels.

714

715 **Appendix A**

716 *Simulated water levels for 30 days at Fort Pulaski, U.S. Georgia, for the EOF analysis*



717 **Fig. A.1** Simulated water levels for 30 days at Fort Pulaski, U.S. Georgia, for the EOF analysis and comparisons
 718 with NOAA tide gauge observations and predictions. The model evaluations, including error statistics, are listed in
 719 Appendix C.
 720

721

722 **Appendix B**

723 *Model evaluation metrics for error statistics*

$$\text{Root-mean-square error, RMSE} = \sqrt{\frac{1}{N} \sum_{t=1}^N (s_t - o_t)^2} \quad (\text{B.1})$$

$$\text{Normalized RMSE, NRMSE} = \frac{\text{RMSE}}{\sigma_o} \quad (\text{B.2})$$

$$\text{Mean bias error, MBE} = \frac{1}{N} \sum_{t=1}^N (s_t - o_t) \quad (\text{B.3})$$

$$\text{Pearson's correlation coefficient, R} = \frac{\sum_{t=1}^N (s_t - \bar{s})(o_t - \bar{o})}{\sqrt{\sum_{t=1}^N (s_t - \bar{s})^2 \sum_{t=1}^N (o_t - \bar{o})^2}} \quad (\text{B.4})$$

$$\text{Nash-Sutcliffe efficiency, NSE} = 1 - \frac{\sum_{t=1}^N (s_t - o_t)^2}{\sum_{t=1}^N (o_t - \bar{o})^2} \quad (\text{B.5})$$

724 where s is the model estimations, o is the actual values, such as observations, and N is the number of
 725 samples. The $\bar{\cdot}$ and σ denote the mean and standard deviation, respectively.

726

727 **Appendix C**

728 *Model evaluations with observations for Fig. 2b, Fig. 10, and Fig. A.1*

729 **Table C.1**730 Model evaluations with observations for Fig. 2b, Fig. 10, and Fig. A.1 (11/25 – 12/25 in 2021). The table index (N1,
731 U1, and S1-6) corresponds to the labels of the station locations in Fig. 1.

Observation Location	SCHISM Model Simulation (Fig. 2b and Fig. A.1)				Physics-based Empirical Modeling Approach (Fig. 10)							
					Reconstructions by EOFs (SSLS)				Cross-Validation excl. Own Sensor			
	RMSE [m]	MBE [m]	R [-]	NSE [-]	RMSE [m]	MBE [m]	R [-]	NSE [-]	RMSE [m]	MBE [m]	R [-]	NSE [-]
NOAA: N1	0.142	-0.129	0.989	0.947	0.084	-0.057	0.995	0.979	-	-	-	-
USGS: U1	0.222	-0.104	0.963	0.907	0.116	-0.110	0.998	0.977	-	-	-	-
SSLS: S1	0.312	-0.012	0.914	0.829	0.096	0.030	0.993	0.984	0.091	0.023	0.990	0.979
SSLS: S2	0.197	0.136	0.984	0.928	0.208	0.178	0.989	0.920	0.228	0.217	0.982	0.877
SSLS: S3	0.359	0.002	0.801	0.642	0.188	0.184	0.998	0.902	0.187	0.187	0.998	0.898
SSLS: S4	0.287	0.016	0.934	0.871	0.048	0.026	0.999	0.996	0.057	0.014	0.997	0.992
SSLS: S5	0.384	0.095	0.851	0.672	0.228	0.205	0.994	0.884	0.297	0.260	0.977	0.751
SSLS: S6	0.539	0.059	0.646	0.407	0.209	0.196	0.995	0.911	0.193	0.181	0.991	0.914

* RMSE: root-mean-square errors, MBE: mean bias errors, R: correlation coefficients, and NSE: Nash-Sutcliffe efficiency.

732

733 **Data availability**

734 The SSLS measurement data can be accessed publicly at <https://www.sealevelsensors.org/>. The DEM,
735 water level, oceanographic, and meteorological data are available through the following links:
736 - DEM data: NOAA Digital Coast (<https://coast.noaa.gov/dataviewer/>)
737 - Water level data: NOAA Tide & Currents (<https://tidesandcurrents.noaa.gov/>), USGS National Water
738 Dashboard (<https://dashboard.waterdata.usgs.gov/>), and USGS Flood Event Viewer
739 (<https://stn.wim.usgs.gov/>)
740 - Oceanographic data: AVISO (<https://www.aviso.altimetry.fr/en/data/products.html>) and CEMES
741 (<https://data.marine.copernicus.eu/products>)
742 - Meteorological data: ECMWF ERA 5 (<https://www.ecmwf.int/en/forecasts/datasets>) and NOAA HRRR
743 (<https://rapidrefresh.noaa.gov/hrrr/>)
744 The SCHISM simulation and Objective Analysis data can be provided upon request to the corresponding
745 author.

746

747 **CRediT author statement**

748 **Youngjun Son**: Conceptualization, Methodology, Software, Validation, Formal analysis, Investigation,
749 Writing – original draft, Writing – review & editing, Visualization. **Emanuele Di Lorenzo**:
750 Conceptualization, Methodology, Investigation, Writing – review & editing, Supervision, Project
751 administration, Funding acquisition. **Kyungmin Park**: Software, Validation, Writing – review & editing.
752 **Spenser Wipperfurth**: Software, Validation, Writing – review & editing. **Jian Luo**: Methodology,
753 Writing – review & editing, Supervision.

754

755 **Acknowledgments**

756 This research is funded by the NOAA Coastal Infrastructure and Resilience Research Initiative: The
757 Georgia Coastal Equity and Resilience (CEAR) Hub project (NA22NOS4690219). We would like to
758 thank Dr. Russell Clark, Kait Morano, Mangesh Atpadikar, Bhargav Singam, Vaishnavi Kulkarni at
759 Georgia Institute of Technology, and Randall Mathews of the Chatham Emergency Management Agency
760 (CEMA) for helping in establishing the real-time application in a pilot web-based CEMA portal. The
761 authors are grateful to the anonymous reviewers for providing insightful and constructive feedback.

762

763 **References**

- 764 Al Kajbaf, A. and Bensi, M., 2020. Application of surrogate models in estimation of storm surge: A
765 comparative assessment. *Applied Soft Computing*, 91.
766 <https://doi.org/10.1016/j.asoc.2020.106184>
- 767 Allen, T.R. et al., 2018. Linking Water Infrastructure, Public Health, and Sea Level Rise: Integrated
768 Assessment of Flood Resilience in Coastal Cities. *Public Works Management & Policy*, 24(1):
769 110-139. <https://doi.org/10.1177/1087724x18798380>
- 770 Asher, T.G., Luettich, R.A., Fleming, J.G. and Blanton, B.O., 2019. Low frequency water level correction
771 in storm surge models using data assimilation. *Ocean Model*, 144.
772 <https://doi.org/10.1016/j.ocemod.2019.101483>
- 773 Avila, L.A., Stewart, S.R., Berg, R. and Hagen, A.B., 2020. Hurricane Dorian 2019, National Hurricane
774 Center. https://www.nhc.noaa.gov/data/tcr/AL052019_Dorian.pdf
- 775 Barnes, S.L., 1964. A Technique for Maximizing Details in Numerical Weather Map Analysis. *Journal of
776 Applied Meteorology*, 3(4): 396-409. [https://doi.org/10.1175/1520-0450\(1964\)003<0396:Atfmdi>2.0.Co;2](https://doi.org/10.1175/1520-0450(1964)003<0396:Atfmdi>2.0.Co;2)
- 777 Bass, B. and Bedient, P., 2018. Surrogate modeling of joint flood risk across coastal watersheds. *Journal
779 of Hydrology*, 558: 159-173. <https://doi.org/10.1016/j.jhydrol.2018.01.014>
- 780 Bilskie, M.V., Hagen, S.C. and Medeiros, S.C., 2020. Unstructured finite element mesh decimation for
781 real-time Hurricane storm surge forecasting. *Coast Eng*, 156.
782 <https://doi.org/10.1016/j.coastaleng.2019.103622>
- 783 Bilskie, M.V. et al., 2021. Enhancing Flood Hazard Assessments in Coastal Louisiana Through Coupled
784 Hydrologic and Surge Processes. *Frontiers in Water*, 3. <https://doi.org/10.3389/frwa.2021.609231>
- 785 Bretherton, F.P., Davis, R.E. and Fandry, C.B., 1976. A technique for objective analysis and design of
786 oceanographic experiments applied to MODE-73. *Deep Sea Research and Oceanographic
787 Abstracts*, 23(7): 559-582. [https://doi.org/10.1016/0011-7471\(76\)90001-2](https://doi.org/10.1016/0011-7471(76)90001-2)
- 788 Chambers, D.P., Mehlhaff, C.A., Urban, T.J., Fujii, D. and Nerem, R.S., 2002. Low-frequency variations
789 in global mean sea level: 1950-2000. *J Geophys Res-Oceans*, 107(C4).
790 <https://doi.org/10.1029/2001jc001089>
- 791 Church, J.A. and White, N.J., 2006. A 20th century acceleration in global sea-level rise. *Geophys Res
792 Lett*, 33(1). <https://doi.org/10.1029/2005gl024826>
- 793 Church, J.A., White, N.J., Coleman, R., Lambeck, K. and Mitrovica, J.X., 2004. Estimates of the
794 Regional Distribution of Sea Level Rise over the 1950–2000 Period. *Journal of Climate*, 17(13):
795 2609-2625. [https://doi.org/10.1175/1520-0442\(2004\)017<2609:Eotrdo>2.0.Co;2](https://doi.org/10.1175/1520-0442(2004)017<2609:Eotrdo>2.0.Co;2)

- 796 Daley, R., 1991. Atmospheric Data Analysis. Cambridge Atmospheric and Space Science Serie.
797 Cambridge University Press, 457 pp.
- 798 Gallien, T.W., Schubert, J.E. and Sanders, B.F., 2011. Predicting tidal flooding of urbanized embayments:
799 A modeling framework and data requirements. *Coast Eng*, 58(6): 567-577.
800 <https://doi.org/10.1016/j.coastaleng.2011.01.011>
- 801 Gold, A.C., Brown, C.M., Thompson, S.P. and Piehler, M.F., 2022. Inundation of Stormwater
802 Infrastructure Is Common and Increases Risk of Flooding in Coastal Urban Areas Along the US
803 Atlantic Coast. *Earth's Future*, 10(3). <https://doi.org/10.1029/2021ef002139>
- 804 Gorry, P.A., 1990. General least-squares smoothing and differentiation by the convolution (Savitzky-
805 Golay) method. *Analytical Chemistry*, 62(6): 570-573. <https://doi.org/10.1021/ac00205a007>
- 806 Grinsted, A., Ditlevsen, P. and Christensen, J.H., 2019. Normalized US hurricane damage estimates using
807 area of total destruction, 1900-2018. *Proc Natl Acad Sci U S A*, 116(48): 23942-23946.
808 <https://doi.org/10.1073/pnas.1912277116>
- 809 Habel, S., Fletcher, C.H., Anderson, T.R. and Thompson, P.R., 2020. Sea-Level Rise Induced Multi-
810 Mechanism Flooding and Contribution to Urban Infrastructure Failure. *Sci Rep*, 10(1): 3796.
811 <https://doi.org/10.1038/s41598-020-60762-4>
- 812 Hallegatte, S., Green, C., Nicholls, R.J. and Corfee-Morlot, J., 2013. Future flood losses in major coastal
813 cities. *Nat Clim Change*, 3(9): 802-806. <https://doi.org/10.1038/nclimate1979>
- 814 Hamlington, B.D., Leben, R.R., Nerem, R.S., Han, W. and Kim, K.Y., 2011. Reconstructing sea level
815 using cyclostationary empirical orthogonal functions. *Journal of Geophysical Research*, 116(C12).
816 <https://doi.org/10.1029/2011jc007529>
- 817 Hamlington, B.D., Leben, R.R., Wright, L.A. and Kim, K.Y., 2012. Regional Sea Level Reconstruction in
818 the Pacific Ocean. *Marine Geodesy*, 35(sup1): 98-117.
819 <https://doi.org/10.1080/01490419.2012.718210>
- 820 Ide, K., Courtier, P., Ghil, M. and Lorenc, A.C., 1997. Unified Notation for Data Assimilation :
821 Operational, Sequential and Variational (gtSpecial IssuetData Assimilation in Meteology and
822 Oceanography: Theory and Practice). *Journal of the Meteorological Society of Japan. Ser. II*,
823 75(1B): 181-189. https://doi.org/10.2151/jmsj1965.75.1B_181
- 824 Integrated Ocean Observing System, 2021. Manual for Real-Time Quality Control of Water Level Data.
825 https://cdn.ioos.noaa.gov/media/2021/04/QARTOD_WaterLevelManual_Update_V2.1_Final.pdf
- 826 Jia, G. and Taflanidis, A.A., 2013. Kriging metamodeling for approximation of high-dimensional wave
827 and surge responses in real-time storm/hurricane risk assessment. *Computer Methods in Applied
828 Mechanics and Engineering*, 261: 24-38. <https://doi.org/10.1016/j.cma.2013.03.012>

- 829 Jia, G. et al., 2015. Surrogate modeling for peak or time-dependent storm surge prediction over an
830 extended coastal region using an existing database of synthetic storms. *Nat Hazards*, 81(2): 909-
831 938. <https://doi.org/10.1007/s11069-015-2111-1>
- 832 Kalnay, E., 2003. *Atmospheric Modeling, Data Assimilation and Predictability*. Cambridge University
833 Press, 341 pp.
- 834 Kaplan, A., Kushnir, Y. and Cane, M.A., 2000. Reduced Space Optimal Interpolation of Historical
835 Marine Sea Level Pressure: 1854–1992*. *Journal of Climate*, 13(16): 2987-3002.
836 [https://doi.org/10.1175/1520-0442\(2000\)013<2987:Rsoioh>2.0.Co;2](https://doi.org/10.1175/1520-0442(2000)013<2987:Rsoioh>2.0.Co;2)
- 837 Karamouz, M., Razmi, A., Nazif, S. and Zahmatkesh, Z., 2017. Integration of inland and coastal storms
838 for flood hazard assessment using a distributed hydrologic model. *Environmental Earth Sciences*,
839 76(11). <https://doi.org/10.1007/s12665-017-6722-6>
- 840 Kerr, P.C. et al., 2013. U.S. IOOS coastal and ocean modeling testbed: Inter-model evaluation of tides,
841 waves, and hurricane surge in the Gulf of Mexico. *Journal of Geophysical Research: Oceans*,
842 118(10): 5129-5172. <https://doi.org/10.1002/jgrc.20376>
- 843 Kim, K.Y., Hamlington, B.D. and Na, H., 2015. Theoretical foundation of cyclostationary EOF analysis
844 for geophysical and climatic variables: Concepts and examples. *Earth-Science Reviews*, 150:
845 201-218. <https://doi.org/10.1016/j.earscirev.2015.06.003>
- 846 Kumar, P., Hamlington, B., Cheon, S.H., Han, W. and Thompson, P., 2020. 20th Century Multivariate
847 Indian Ocean Regional Sea Level Reconstruction. *Journal of Geophysical Research: Oceans*,
848 125(10). <https://doi.org/10.1029/2020jc016270>
- 849 Kyprioti, A.P. et al., 2023. Spatio-temporal storm surge emulation using Gaussian Process techniques.
850 *Coast Eng*, 180. <https://doi.org/10.1016/j.coastaleng.2022.104231>
- 851 Li, M., Wang, R.-Q. and Jia, G., 2020. Efficient dimension reduction and surrogate-based sensitivity
852 analysis for expensive models with high-dimensional outputs. *Reliability Engineering & System
853 Safety*, 195. <https://doi.org/10.1016/j.ress.2019.106725>
- 854 Li, S. et al., 2021. Evolving tides aggravate nuisance flooding along the U.S. coastline. *Sci Adv*, 7(10).
855 <https://doi.org/10.1126/sciadv.abe2412>
- 856 Llovel, W., Cazenave, A., Rogel, P., Lombard, A. and Nguyen, M.B., 2009. Two-dimensional
857 reconstruction of past sea level (1950–2003) from tide gauge data and an Ocean General
858 Circulation Model. *Climate of the Past*, 5(2): 217-227. <https://doi.org/10.5194/cp-5-217-2009>
- 859 Loftis, D. et al., 2018. StormSense: A New Integrated Network of IoT Water Level Sensors in the Smart
860 Cities of Hampton Roads, VA. *Mar Technol Soc J*, 52. <https://doi.org/10.4031/MTSJ.52.2.7>

- 861 Madsen, K.S., Hoyer, J.L., Fu, W. and Donlon, C., 2015. Blending of satellite and tide gauge sea level
862 observations and its assimilation in a storm surge model of the North Sea and Baltic Sea. *J
863 Geophys Res-Oceans*, 120(9): 6405-6418. <https://doi.org/10.1002/2015jc011070>
- 864 Marsooli, R., Orton, P.M., Georgas, N. and Blumberg, A.F., 2016. Three-dimensional hydrodynamic
865 modeling of coastal flood mitigation by wetlands. *Coast Eng*, 111: 83-94.
866 <https://doi.org/10.1016/j.coastaleng.2016.01.012>
- 867 Meyssinac, B. et al., 2011. Two-dimensional reconstruction of the Mediterranean sea level over 1970–
868 2006 from tide gage data and regional ocean circulation model outputs. *Global and Planetary
869 Change*, 77(1-2): 49-61. <https://doi.org/10.1016/j.gloplacha.2011.03.002>
- 870 MODIS Land Rapid Response Team and NASA GSFC, 2019. September 7, 2019 - Hurricane Dorian.
871 https://modis.gsfc.nasa.gov/gallery/individual.php?db_date=2019-09-07 (Accessed 05/23/2023).
- 872 Moftakhar, H.R., AghaKouchak, A., Sanders, B.F., Allaire, M. and Matthew, R.A., 2018. What Is
873 Nuisance Flooding? Defining and Monitoring an Emerging Challenge. *Water Resour Res*, 54(7):
874 4218-4227. <https://doi.org/10.1029/2018wr022828>
- 875 Moftakhar, H.R. et al., 2015. Increased nuisance flooding along the coasts of the United States due to sea
876 level rise: Past and future. *Geophys Res Lett*, 42(22): 9846-9852.
877 <https://doi.org/10.1002/2015gl066072>
- 878 Moore, F.C. and Obradovich, N., 2020. Using remarkable to define coastal flooding thresholds. *Nat
879 Commun*, 11(1): 530. <https://doi.org/10.1038/s41467-019-13935-3>
- 880 Muis, S., Verlaan, M., Winsemius, H.C., Aerts, J.C. and Ward, P.J., 2016. A global reanalysis of storm
881 surges and extreme sea levels. *Nat Commun*, 7: 11969. <https://doi.org/10.1038/ncomms11969>
- 882 Muñoz, D.F., Abbaszadeh, P., Moftakhar, H. and Moradkhani, H., 2022. Accounting for uncertainties in
883 compound flood hazard assessment: The value of data assimilation. *Coast Eng*, 171.
884 <https://doi.org/10.1016/j.coastaleng.2021.104057>
- 885 Muñoz, D.F., Muñoz, P., Moftakhar, H.R. and Moradkhani, H., 2021. From local to regional compound
886 flood mapping with deep learning and data fusion techniques. *Science of The Total Environment*,
887 782. <https://doi.org/10.1016/j.scitotenv.2021.146927>
- 888 National Academies, 2014. Reducing Coastal Risk on the East and Gulf Coasts, Washington, DC, USA.
889 [https://nap.nationalacademies.org/catalog/18811/reducing-coastal-risk-on-the-east-and-gulf-
coasts](https://nap.nationalacademies.org/catalog/18811/reducing-coastal-risk-on-the-east-and-gulf-
890 coasts)
- 891 NOAA NWS, 2016. National Water Model. [https://water.noaa.gov/documents/wrn-national-water-
model.pdf](https://water.noaa.gov/documents/wrn-national-water-
892 model.pdf) (Accessed 11/20/2022).
- 893 Pearson, R.K., Neuvo, Y., Astola, J. and Gabbouj, M., 2016. Generalized Hampel Filters. *EURASIP
894 Journal on Advances in Signal Processing*, 2016(1). <https://doi.org/10.1186/s13634-016-0383-6>

- 895 Rohmer, J., Sire, C., Lecacheux, S., Idier, D. and Pedreros, R., 2023. Improved metamodels for predicting
896 high-dimensional outputs by accounting for the dependence structure of the latent variables:
897 application to marine flooding. *Stochastic Environmental Research and Risk Assessment*, 37(8):
898 2919-2941. <https://doi.org/10.1007/s00477-023-02426-z>
- 899 Rong, Y.N. and San Liang, X., 2022. An Information Flow-Based Sea Surface Height Reconstruction
900 Through Machine Learning. *Ieee Transactions on Geoscience and Remote Sensing*, 60: 1-9.
901 <https://doi.org/10.1109/Tgrs.2022.3140398>
- 902 Rucker, C.A. et al., 2021. Downscaling of real-time coastal flooding predictions for decision support. *Nat
903 Hazards*, 107(2): 1341-1369. <https://doi.org/10.1007/s11069-021-04634-8>
- 904 Savitzky, A. and Golay, M.J.E., 1964. Smoothing and Differentiation of Data by Simplified Least
905 Squares Procedures. *Analytical Chemistry*, 36(8): 1627-1639.
906 <https://doi.org/10.1021/ac60214a047>
- 907 Smith, R.A.E., Bates, P.D. and Hayes, C., 2011. Evaluation of a coastal flood inundation model using
908 hard and soft data. *Environmental Modelling & Software*.
909 <https://doi.org/10.1016/j.envsoft.2011.11.008>
- 910 Smith, T.M., Reynolds, R.W., Livezey, R.E. and Stokes, D.C., 1996. Reconstruction of Historical Sea
911 Surface Temperatures Using Empirical Orthogonal Functions. *Journal of Climate*, 9(6): 1403-
912 1420. [https://doi.org/10.1175/1520-0442\(1996\)009<1403:Rohsst>2.0.Co;2](https://doi.org/10.1175/1520-0442(1996)009<1403:Rohsst>2.0.Co;2)
- 913 Son, Y., Di Lorenzo, E. and Luo, J., 2023. WRF-Hydro-CUFA: A scalable and adaptable coastal-urban
914 flood model based on the WRF-Hydro and SWMM models. *Environmental Modelling &
915 Software*, 167. <https://doi.org/10.1016/j.envsoft.2023.105770>
- 916 Spicer, P., Schlichting, D., Huguenard, K., Roche, A.J. and Rickard, L.N., 2021. Sensing storm surge: A
917 framework for establishing a citizen scientist monitored water level network. *Ocean & Coastal
918 Management*, 211. <https://doi.org/10.1016/j.ocemoaman.2021.105802>
- 919 Sweet, W.V., Dusek, G., Obeysekera, J. and Marra, J., 2018. Patterns and Projections of High Tide
920 Flooding along the U.S. Coastline using a Common Impact Threshold, National Oceanic and
921 Atmospheric Administration.
922 https://www.tidesandcurrents.noaa.gov/publications/tech rpt86_PaP_of_HTFlooding.pdf
- 923 Sweet, W.V. et al., 2022. Global and Regional Sea Level Rise Scenarios for the United States: Updated
924 Mean Projections and Extreme Water Level Probabilities Along U.S. Coastlines, National
925 Oceanic and Atmospheric Administration.
926 <https://oceanservice.noaa.gov/hazards/sealevelrise/noaa-nostechrpt01-global-regional-SLR-scenarios-US.pdf>

- 928 Sweet, W.V., Park, J., Gill, S. and Marra, J., 2015. New ways to measure waves and their effects at
929 NOAA tide gauges: A Hawaiian-network perspective. *Geophys Res Lett*, 42(21): 9355-9361.
930 <https://doi.org/10.1002/2015gl066030>
- 931 Tahvildari, N. and Castrucci, L., 2021. Relative Sea Level Rise Impacts on Storm Surge Flooding of
932 Transportation Infrastructure. *Natural Hazards Review*, 22(1).
933 [https://doi.org/10.1061/\(asce\)nh.1527-6996.0000412](https://doi.org/10.1061/(asce)nh.1527-6996.0000412)
- 934 Tien, I., Lozano, J.-M. and Chavan, A., 2023. Locating real-time water level sensors in coastal
935 communities to assess flood risk by optimizing across multiple objectives. *Communications Earth
936 & Environment*, 4(1). <https://doi.org/10.1038/s43247-023-00761-1>
- 937 Ubelmann, C., Klein, P. and Fu, L.-L., 2015. Dynamic Interpolation of Sea Surface Height and Potential
938 Applications for Future High-Resolution Altimetry Mapping. *Journal of Atmospheric and
939 Oceanic Technology*, 32(1): 177-184. <https://doi.org/10.1175/jtech-d-14-00152.1>
- 940 Verri, G. et al., 2017. A meteo-hydrological modelling system for the reconstruction of river runoff: the
941 case of the Ofanto river catchment. *Nat Hazard Earth Sys*, 17(10): 1741-1761.
942 <https://doi.org/10.5194/nhess-17-1741-2017>
- 943 Ye, F. et al., 2020. Simulating storm surge and compound flooding events with a creek-to-ocean model:
944 Importance of baroclinic effects. *Ocean Model*, 145.
945 <https://doi.org/10.1016/j.ocemod.2019.101526>
- 946 Zhang, Y. and Baptista, A.M., 2008. SELFE: A semi-implicit Eulerian–Lagrangian finite-element model
947 for cross-scale ocean circulation. *Ocean Model*, 21(3-4): 71-96.
948 <https://doi.org/10.1016/j.ocemod.2007.11.005>
- 949 Zhang, Y.J., Ye, F., Stanev, E.V. and Grashorn, S., 2016. Seamless cross-scale modeling with SCHISM.
950 *Ocean Model*, 102: 64-81. <https://doi.org/10.1016/j.ocemod.2016.05.002>
- 951 Zhang, Y.J. et al., 2020. Simulating compound flooding events in a hurricane. *Ocean Dynamics*, 70(5):
952 621-640. <https://doi.org/10.1007/s10236-020-01351-x>
- 953